Supplementary Information

High-capacity, fast-charging and long-life magnesium/black phosphorous composite negative electrode for non-aqueous magnesium battery

Qiannan Zhao [1, 2, 3], Kaiqi Zhao [1, 2, 4], Gao-Feng Han [5], Ming Huang [6], Ronghua Wang [1, 4, *], Zhiqiao Wang [7], Wang Zhou [8], Yue Ma [7], Jilei Liu [8], Zhongting Wang [1, 4], Chaohe Xu [1, 3, 4*], Guangsheng Huang [1, 4], Jingfeng Wang [1, 4], Fusheng Pan [1, 4], and Jong-Beom Baek [2, *]

[1] *National Engineering Research Center for Magnesium Alloys, Chongqing University, Chongqing, 400044, P.R. China*

[2] *School of Energy and Chemical Engineering, Center for Dimension-Controllable Organic Frameworks, Ulsan National Institute of Science and Technology (UNIST), Ulsan,44919, South Korea*

[3] *College of Aerospace Engineering, Chongqing University, Chongqing, 400044, P.R. China*

[4] *Chongqing Institute of New Energy Storage Materials and Equipment, Chongqing 401135, China*

[5] *Key Laboratory of Automobile Materials, Ministry of Education, and School of Materials Science and Engineering, Jilin University, Changchun 130012, P.R. China*

[6] *Institute of Fundamental and Frontier Sciences, University of Electronic Science and Technology of China, Chengdu 610054, P.R. China*

[7] *School of Materials Science and Engineering Northwestern Polytechnical University and Shaanxi Joint Laboratory of Graphene (NPU) Xi'an 710072, P.R. China*

[8] *College of Materials Science and Engineering, Hunan Joint International Laboratory of Advanced Materials and Technology of Clean Energy, Hunan University, Changsha, Hunan 410082, P.R. China*

***Corresponding Author**

Email: wangrh@cqu.edu.cn (Prof. Ronghua Wang); xche@cqu.edu.cn (Prof. Chaohe Xu); jbbaek@unist.ac.kr (Prof. Jong-Beom Baek)

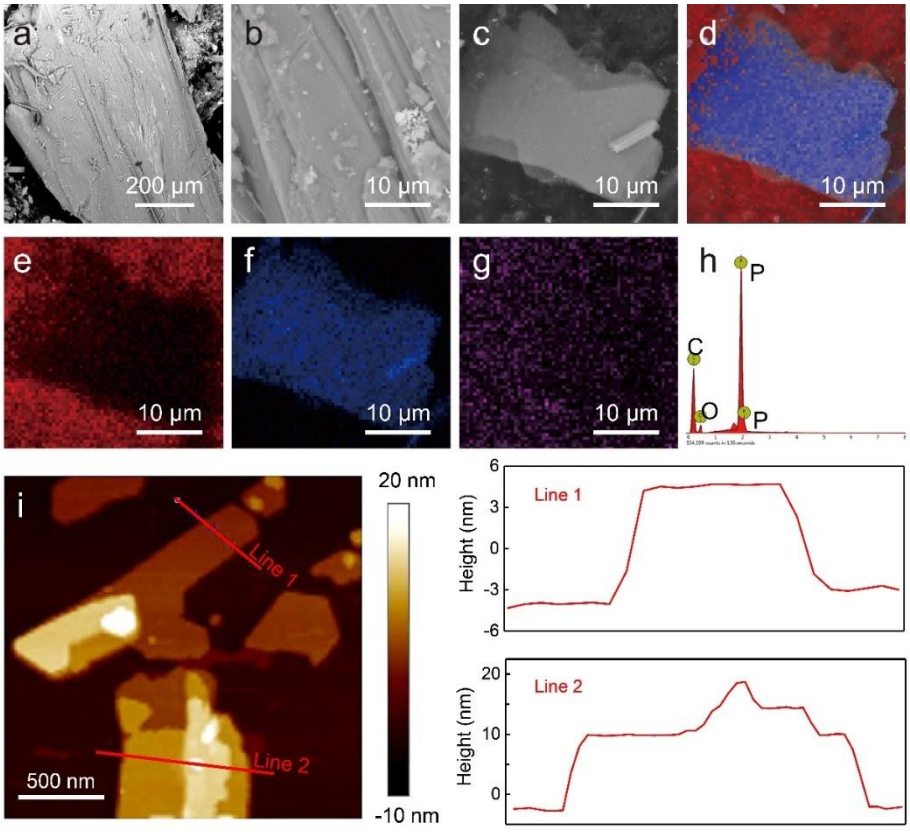

Supplementary Figure 1. Material characterization of BP material. a, **b**, SEM images of bulk BP material before delamination. SEM image and EDS mappings of BP after delamination in NMP. **c**, SEM image. **d**, Merged mapping. **e**–**g**, Corresponding C, P, and O element mappings, respectively. **h**, The EDS spectrum. **i,** AFM images and height profiles of the prepared BP nanosheets.

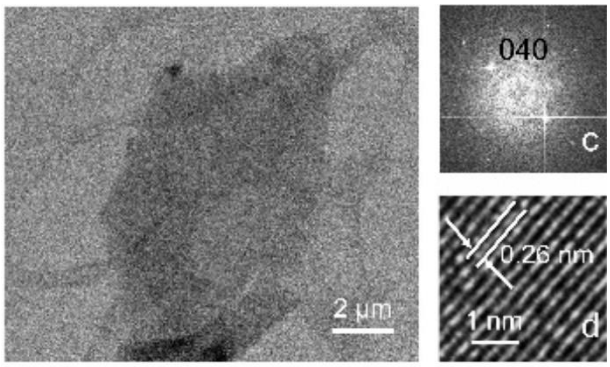

Supplementary Figure 2. TEM image and diffraction patterns of BP nanosheets.

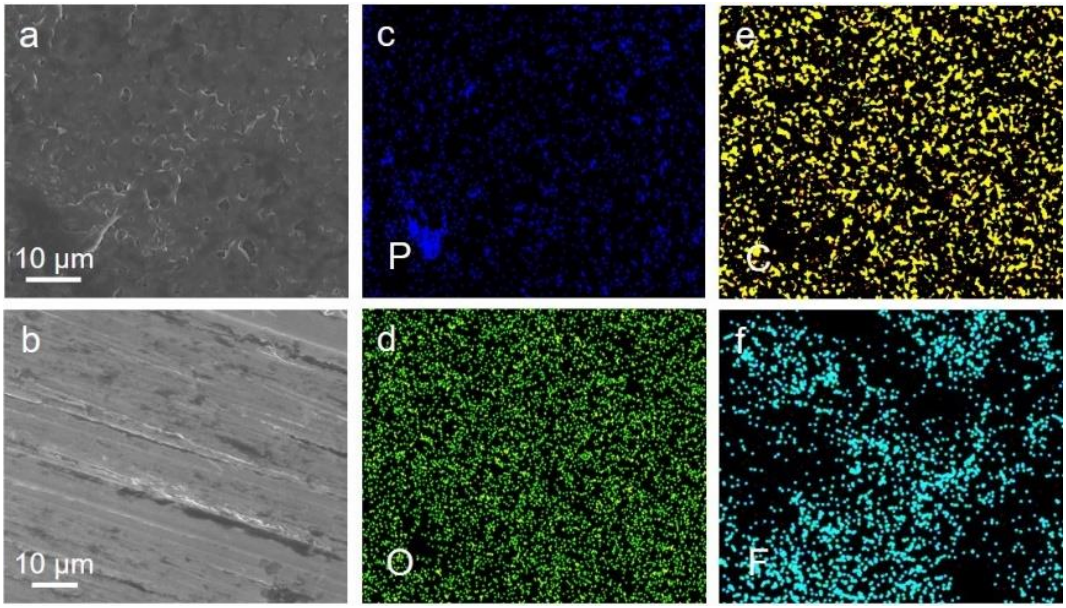

Supplementary Figure 3. Micro-morphology characterization of BP electrode and metal Mg negative electrode. SEM images **a**, BP electrode. **b**, metal Mg negative electrode after polishing. **c**–**f,** Corresponding C, O, F element mappings of the BP electrode.

Supplementary Figure 4. Photograph of the free-standing BP electrode (named as F-BP).

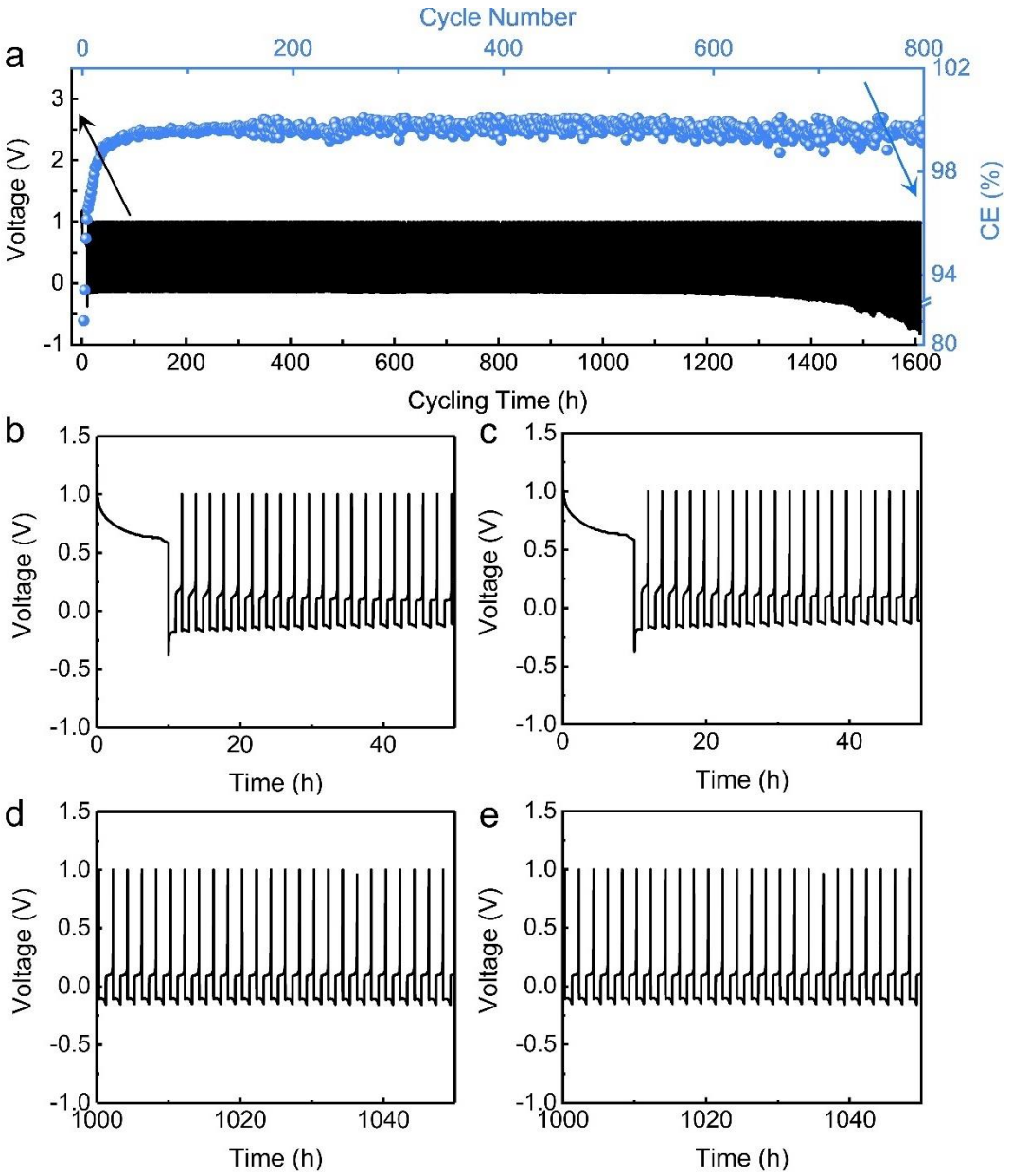

Supplementary Figure 5. Plating/stripping performances of asymmetric Mg||BP coin cell configuration at I_D of 2 mA cm^{-2} and area capacity of 2 mAh cm^{-2}. a, Cycling performance. **b**–**e**, Partial enlarged views of the cycling profile. The test was conducted at 25 °C.

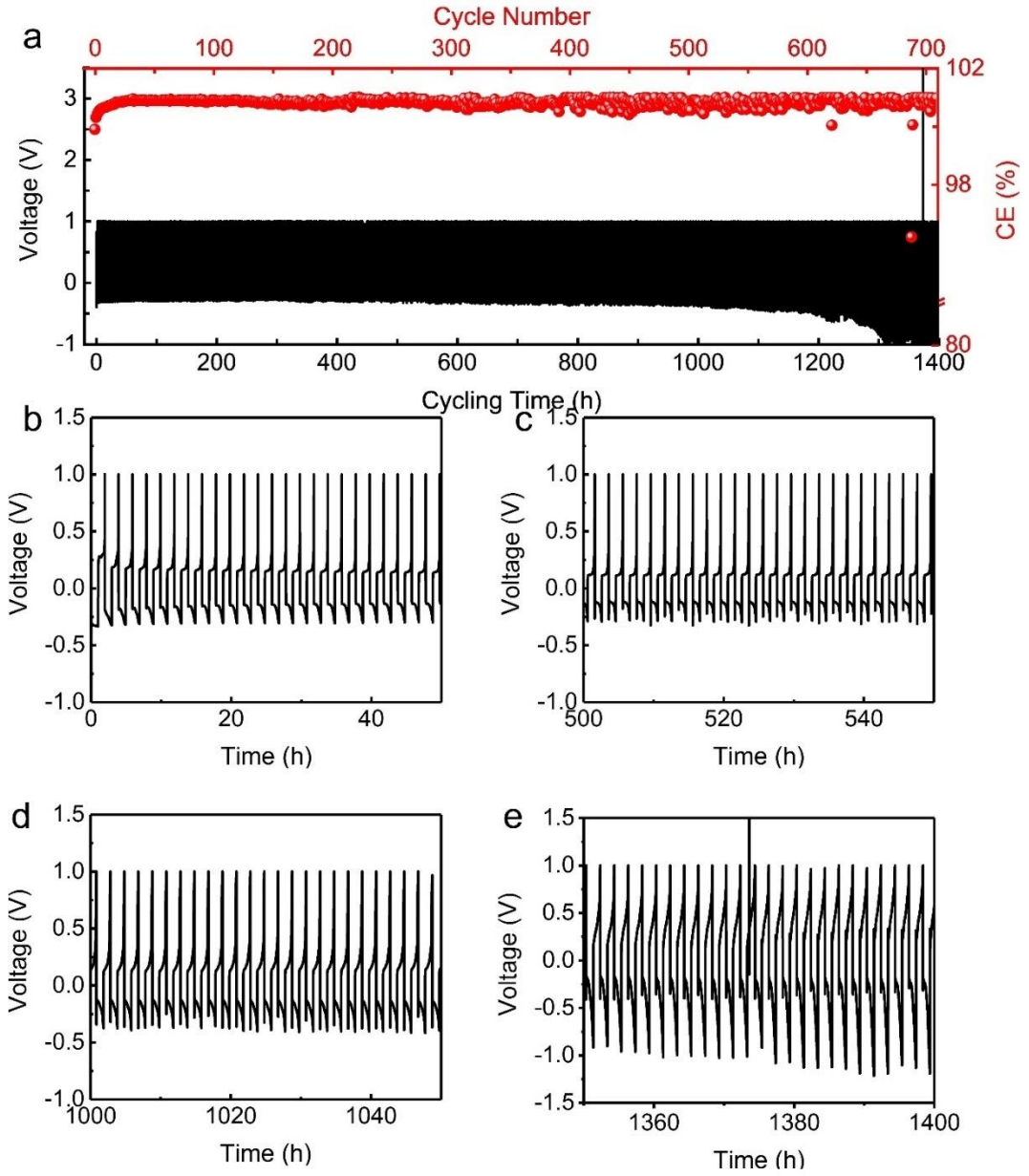

Supplementary Figure 6. Plating/stripping performances of asymmetric Mg||BP coin cell configuration at I_D of 4 mA cm^{-2} and area capacity of 4 mAh cm^{-2}. a, Cycling performance. **b**–**e**, Partial enlarged views of the cycling profile. The test was conducted at 25 °C using an APC electrolyte solution.

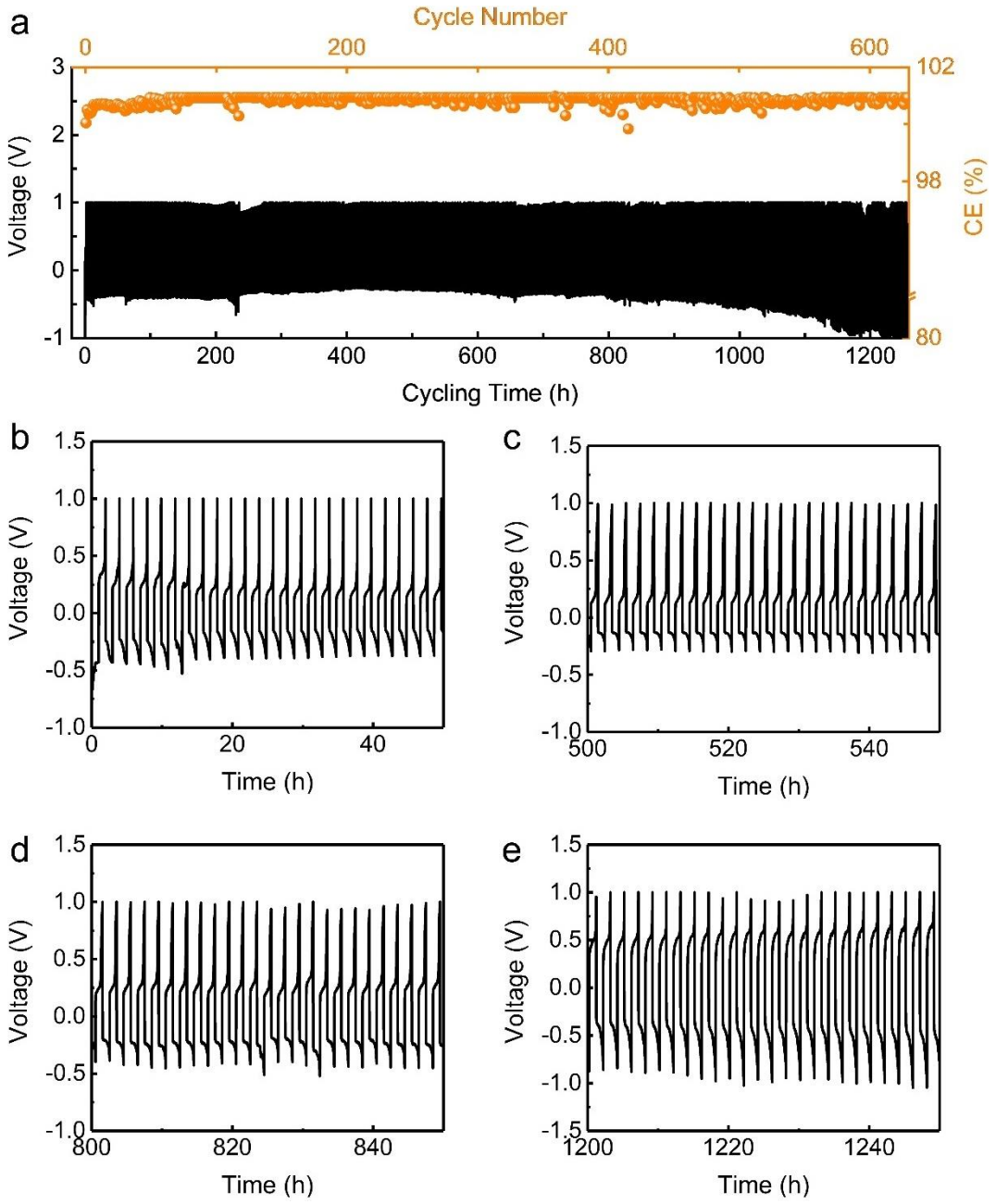

Supplementary Figure 7. Plating/stripping performances of asymmetric Mg||BP coin cell configuration at I_D of 8 mA cm^{-2} and area capacity of 8 mAh cm^{-2}. a, Cycling performance. **b**–**e**, Partial enlarged views of the cycling profile. The test was conducted at 25 °C using an APC electrolyte solution.

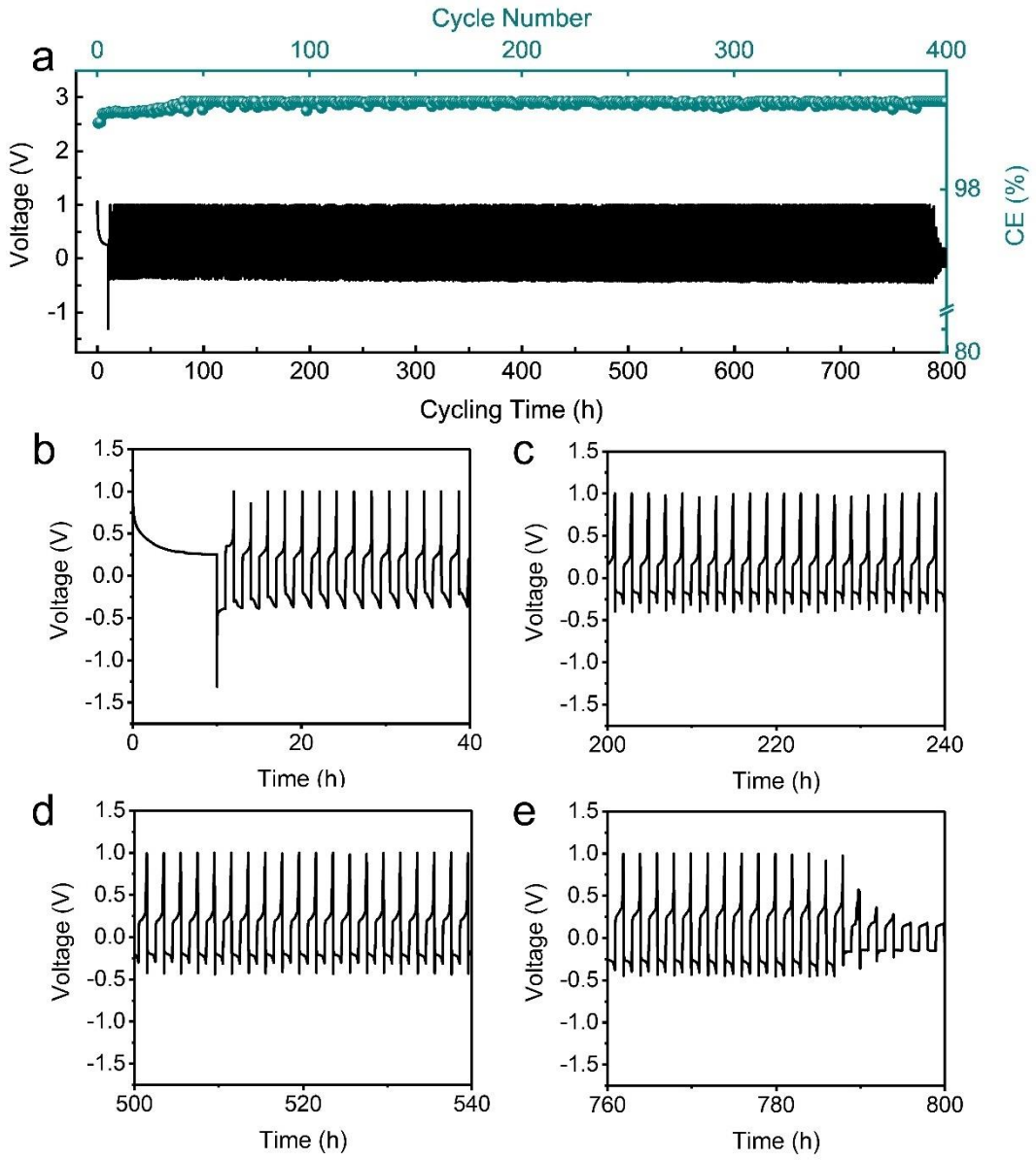

Supplementary Figure 8. Plating/stripping performances of asymmetric Mg||BP coin cell at I_D of 16 mA cm^{-2} and area capacity of 16 mAh cm^{-2}. a, Cycling performance. **b**–**e**, Partial enlarged views of the cycling profiles. The test was conducted at 25 °C using an APC electrolyte solution.

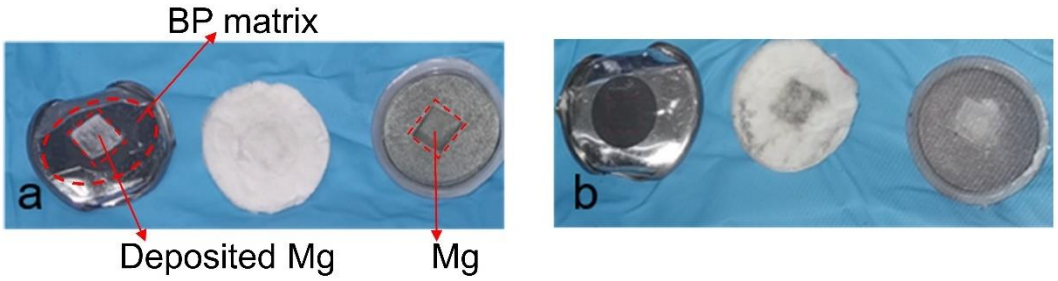

Supplementary Figure 9. Optical photographs of disassembled Mg||BP coin cells. a, After Mg depositing. **b**, After Mg stripping from the Mg@BP electrode. The test was conducted at 25 °C using an APC electrolyte solution.

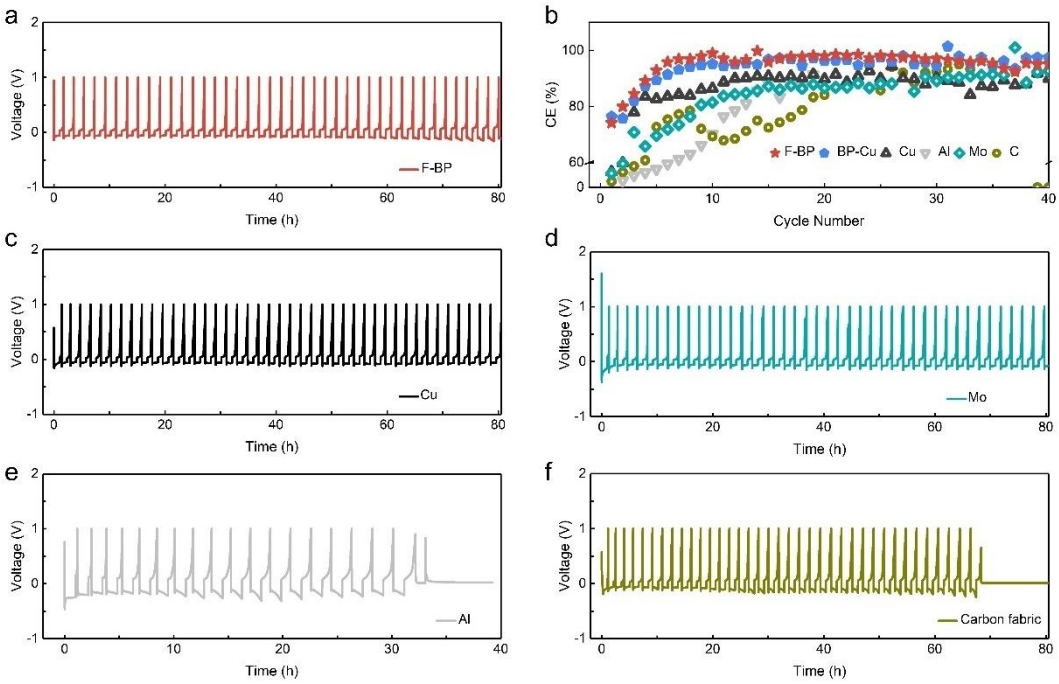

Supplementary Figure 10. Mg deposition and stripping performances of free-standing BP (F-BP), Cu, Al, Mo, and Carbon fabric (C) substrates. Cycling performances of the asymmetric cells: **a**, F-BP||Mg, **c**, Cu||Mg, **d**, Mo||Mg, **e**, Al||Mg, and **f**, C||Mg cells. **b**, Corresponding CEs of the above asymmetric batteries during cycling. The testing condition was set at I_D of 0.5 mA cm^{-2} and C_a of 0.5 mAh cm^{-2}. The test was conducted at 25 °C using an APC electrolyte solution.

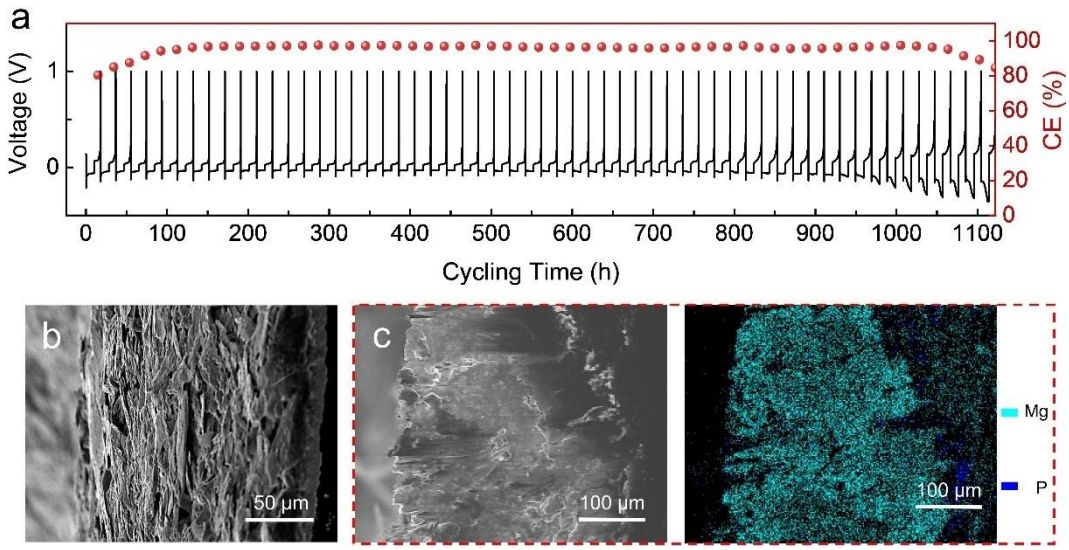

Supplementary Figure 11. Fabrication of the Mg@BP with ultra-large deposition capacity. **a**, Cycling performance of the asymmetric BP||Mg cell at I_D of 8.0 mA cm^{-2} and area capacity of 80.0 mAh cm^{-2}. **b**, Cross-section micro-image of the BP electrode for preparing the high-capacity Mg@BP composite negative electrode. **c**, Cross-section micro-image and EDS mappings of the Mg@BP composite negative electrode with deposited capacity of 80.0 mAh cm^{-2}. The test was conducted at 25 °C using an APC electrolyte solution.

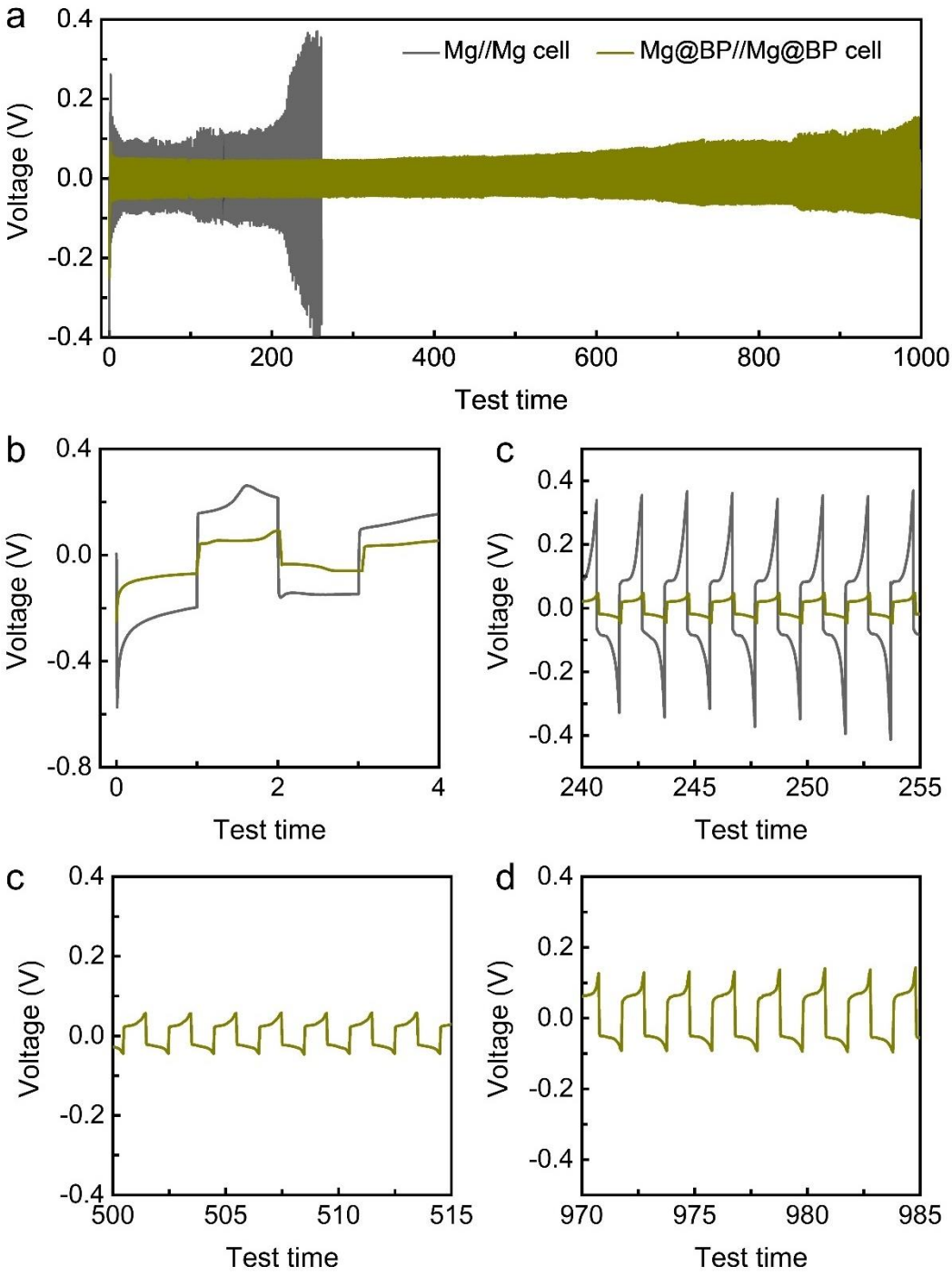

Supplementary Figure 12. Electrochemical performances of the symmetric Mg@BP||Mg@BP and symmetric Mg||Mg cells at 0.9 mA cm^{-2} and 0.9 mAh cm^{-2} (90% DOD). a, Voltage profiles of the of the symmetric Mg@BP||Mg@BP cell and symmetric Mg||Mg battery during cycling. **b**–**d**, Enlarged voltage profiles of **a**. The test was conducted at 25 °C using an APC electrolyte solution.

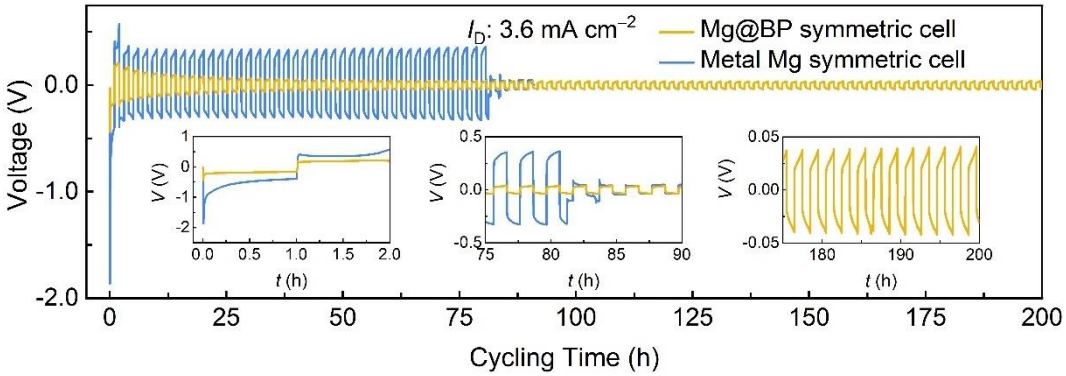

Supplementary Figure 13. Cycling performances of the symmetric Mg@BP cell (90% DOD) and the symmetric Mg cell at I_D of 3.6 mA cm^{-2}. The plated C_a of the Mg@BP composite electrode is 4.0 mAh cm^{-2}. The test was conducted at 25 °C using an APC electrolyte solution.

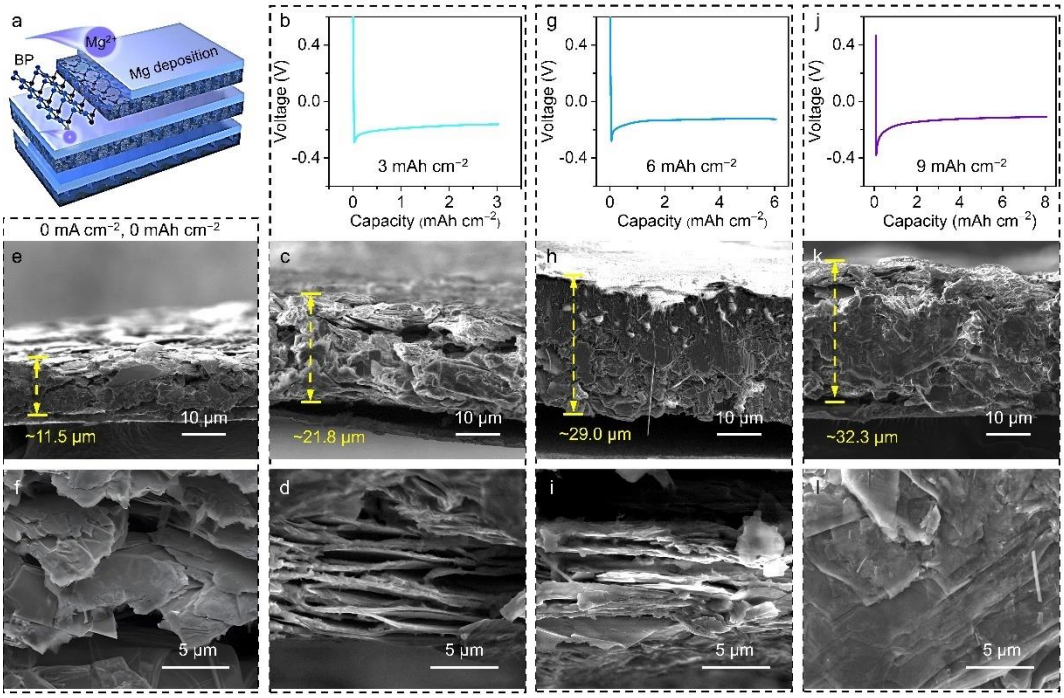

Supplementary Figure 14. Mg plating behavior study of BP electrode from the cross-section view of the BP electrode and Mg@BP composite electrode with different depositing capacity (C_a). a, Scheme illustration of Mg plating behavior. **b**, **g**, **j**, Voltage profiles to prepare the Mg@BP composite electrode with C_a of 3, 6, and 9 mAh cm^{-2}, respectively. SEM cross-section images of **e,** BP electrode and Mg@BP composite electrodes with C_a of **c**, 3, **h**, 6, and **k**, 9 mAh cm^{-2}. **f**, **d**, **i**, **l**, Zoom-in images of **e**-**h**, respectively. The electrochemical tests were conducted at 25 °C using an APC electrolyte solution.

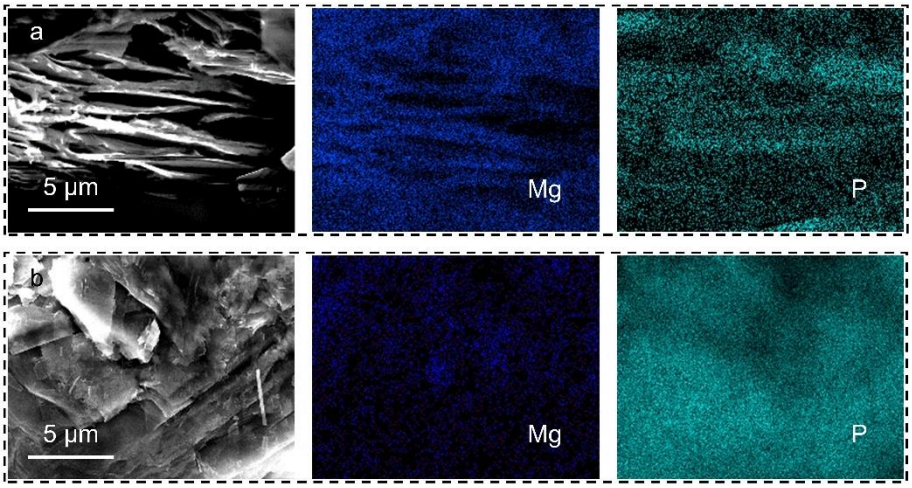

Supplementary Figure 15. SEM images and corresponding EDS mappings of the Mg@BP composite electrodes with different area capacities. a, 3 mAh cm^{-2}. **b**, 9 mAh cm^{-2}. The electrochemical tests were conducted at 25 °C using an APC electrolyte solution.

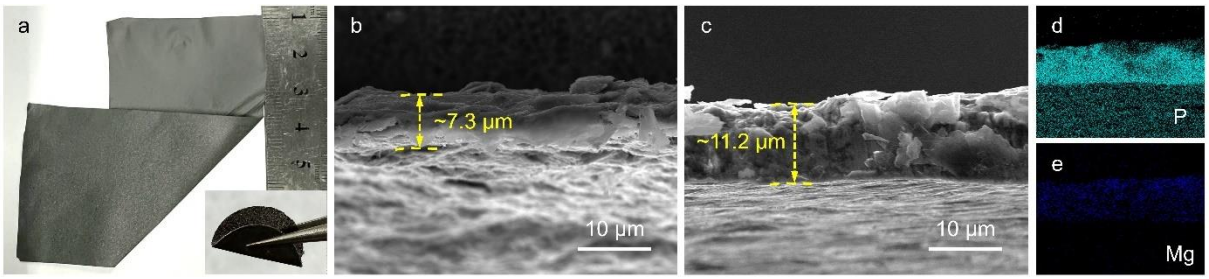

Supplementary Figure 16. Free-standing BP electrode (F-BP) and the as-prepared Mg@F-BP composite electrode. a, Photograph of the prepared F-BP electrode with good flexibility. **b**, SEM cross-section image of the F-BP electrode with thin thickness of about 7.3 μm. **c**, SEM cross-section image and **d**-**e**, EDS mappings of the as-prepared Mg@F-BP composite negative electrode, which showed tense cross-section structure and uniform element P and Mg distributions along the thickness direction. The electrochemical tests were conducted at 25 °C using an APC electrolyte solution.

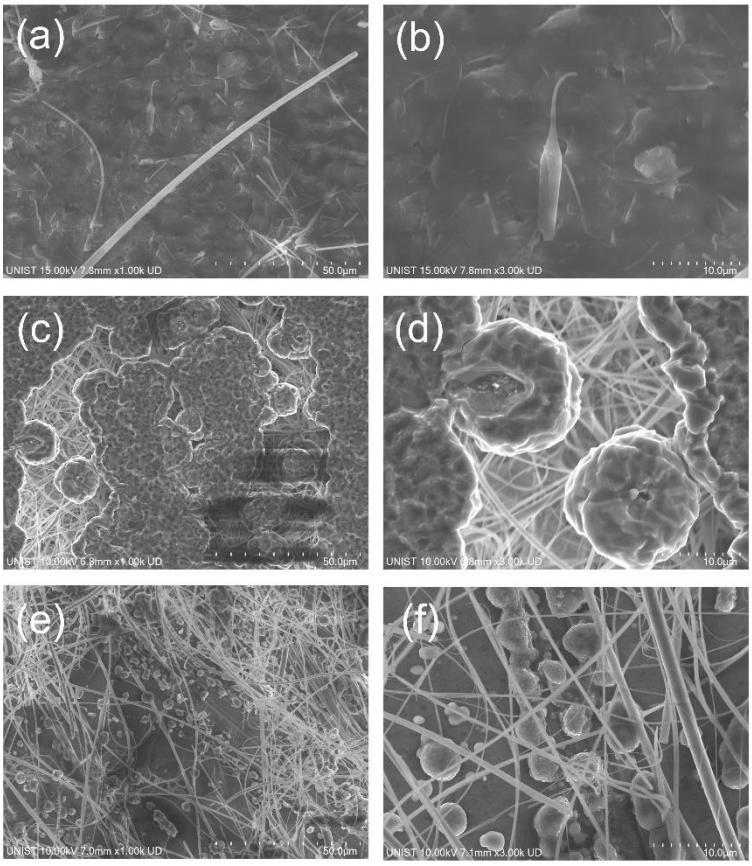

Supplementary Figure 17. Mg deposition morphologies characterized on different substrates with a deposition capacity of 3.0 mAh cm^{-2}. a, **b**, On BP substrate. **c**, **d**, On Cu substrate. **e**, **f**, On metal Mg substrate. The fiber-like structures are residues of the glass fiber separator. The electrochemical tests were conducted at 25 °C using an APC electrolyte solution.

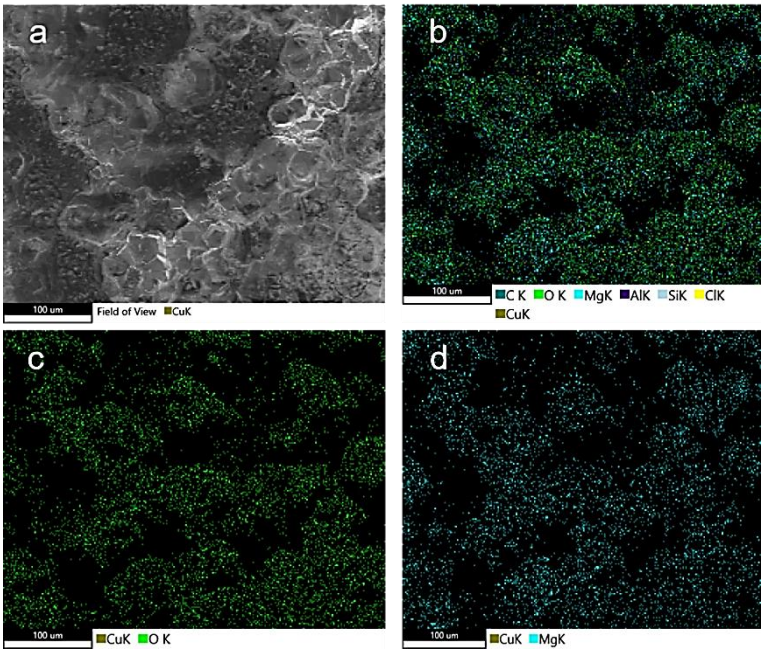

Supplementary Figure 18. SEM and EDS mappings of the Cu matrix after Mg deposition with an area capacity of 3.0 mAh cm^{-2}. The electrochemical tests were conducted at 25 °C using an APC electrolyte solution.

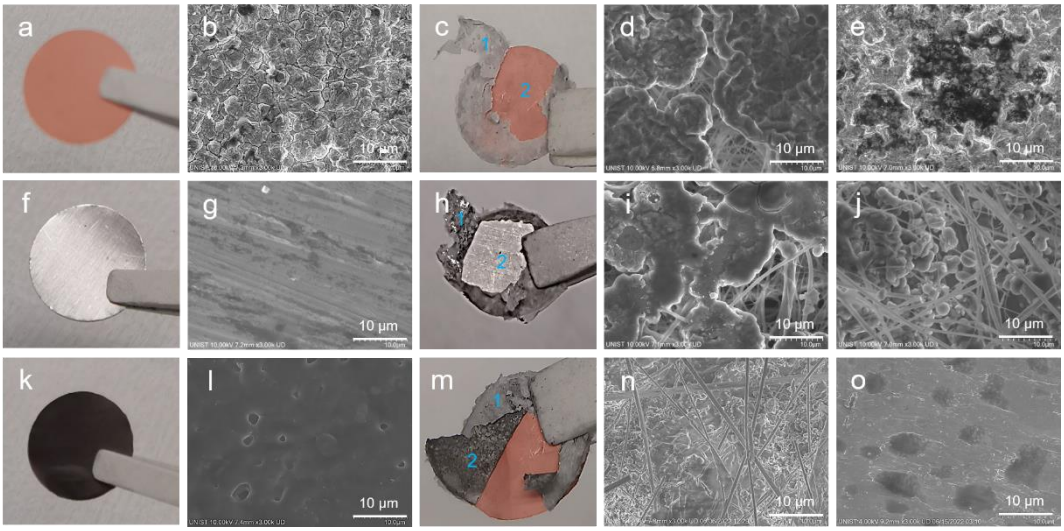

Supplementary Figure 19. Characterization of surface morphologies of different substrates before and after Mg deposition with an area capacity of 5.0 mAh cm^{-2}. **a**–**e**, The Cu substrate. **f**–**j**, The Mg foil. **k**–**o**, The BP matrix. **a**, **f**, **k**, The optical and **b**, **g**, **l**, Surface SEM images of the bare Cu, pristine Mg, and BP, respectively. **c**, **h**, **m**, The optical and **d**, **e**, **i**, **j**, **n**, **o**, Surface SEM images of Cu, Mg, and BP electrode after Mg deposition. **d**, **i**, **n**, The surface morphologies of region 1 in **c**, **h**, **m**, respectively. **e**, **j**, **o**, The surface morphologies of region 2 in **c**, **h**, **m**, respectively. The fiber-like structures are glass fibers. The electrochemical tests were conducted at 25 °C using an APC electrolyte solution.

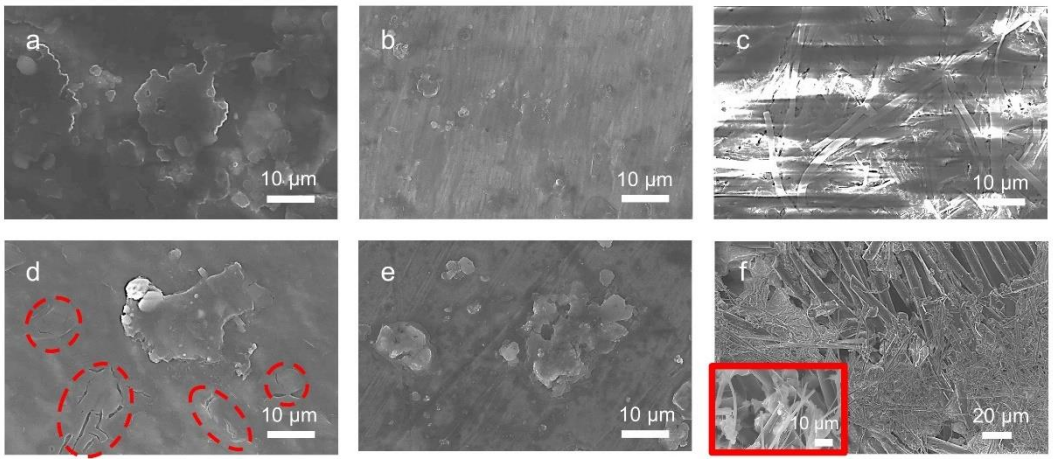

Supplementary Figure 20. Mg deposition morphologies on different substrates. a, Mg@F-BP. **b,** Mg@Cu. **c**, Glass fiber separator used in Cu||Mg cell. **d**, Mg@Al. **e**, Mg@Mo. **f**, Mg@C. The electrochemical tests were conducted at 25 °C using an APC electrolyte solution.

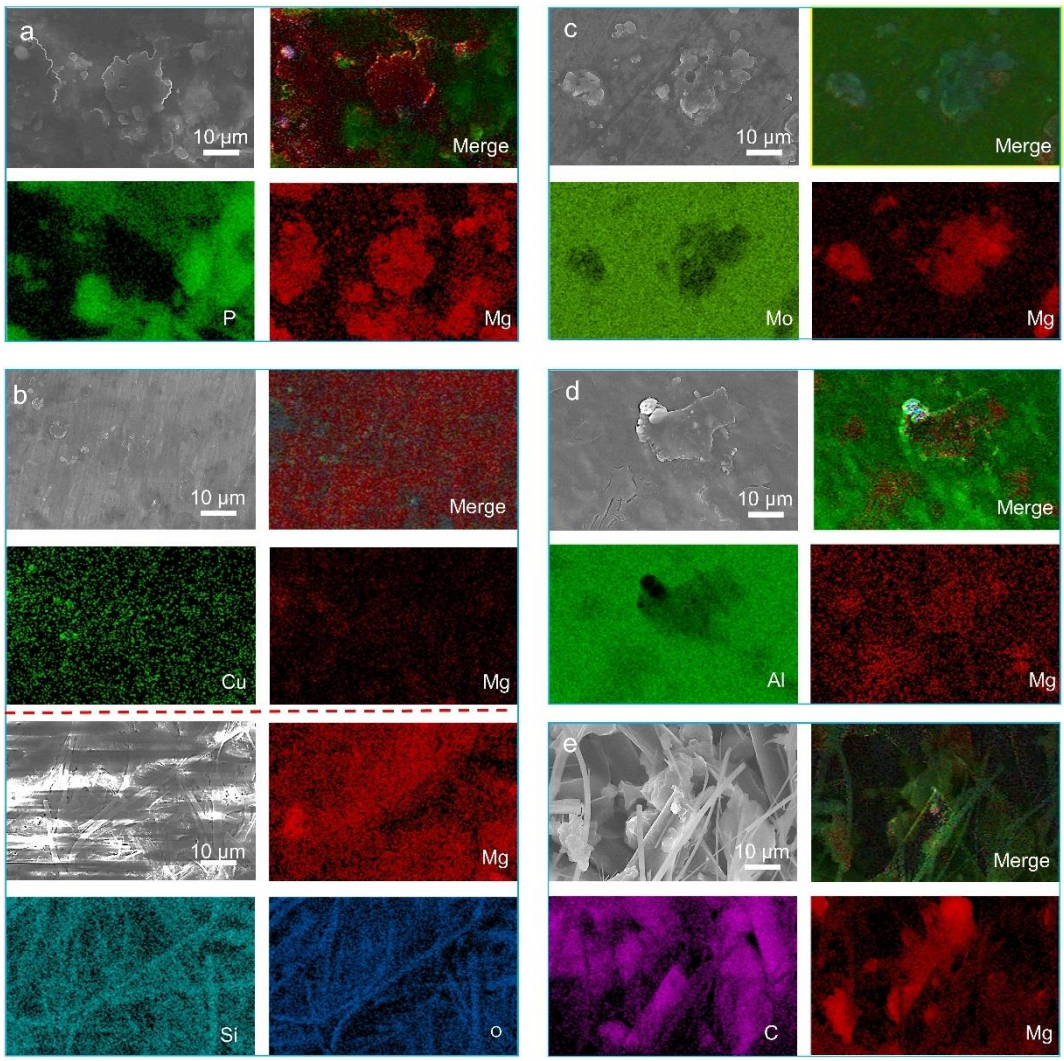

153

154 **Supplementary Figure 21. Morphology and EDS mappings of the Mg composite**
155 **electrodes prepared with different substrates. a**, Mg@F-BP. **b**, Mg@Cu (above the red dash
156 line) and the applied glass fiber separator (below the red dash line). **c**, Mg@Mo. **d**, Mg@Al **e**,
157 Mg@C composite negative electrode. The electrochemical tests were conducted at 25 °C using
158 an APC electrolyte solution.

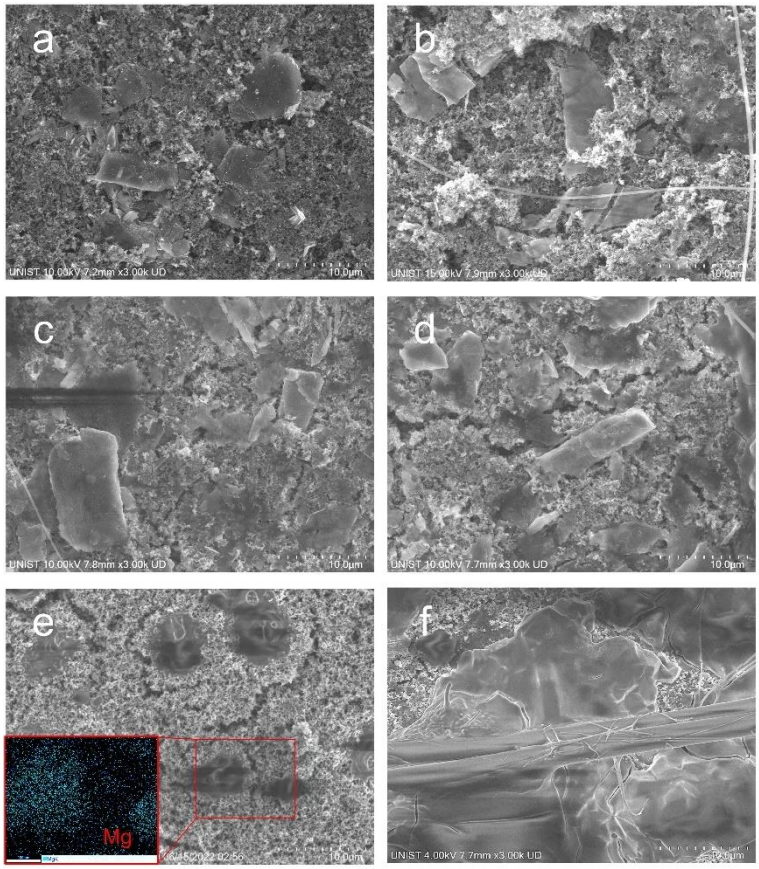

Supplementary Figure 22. Surface morphologies of the cycled BP-carbon electrodes with different Mg depositing capacities. a, 0 mAh cm^{-2}. **b**, 0.125 mAh cm^{-2}. **c**, 0.25 mAh cm^{-2}. **d**, 0.5 mAh cm^{-2}. **e**, 1.0 mAh cm^{-2}. **f**, 5.0 mAh cm^{-2}. The electrochemical tests were conducted at 25 °C using an APC electrolyte solution.

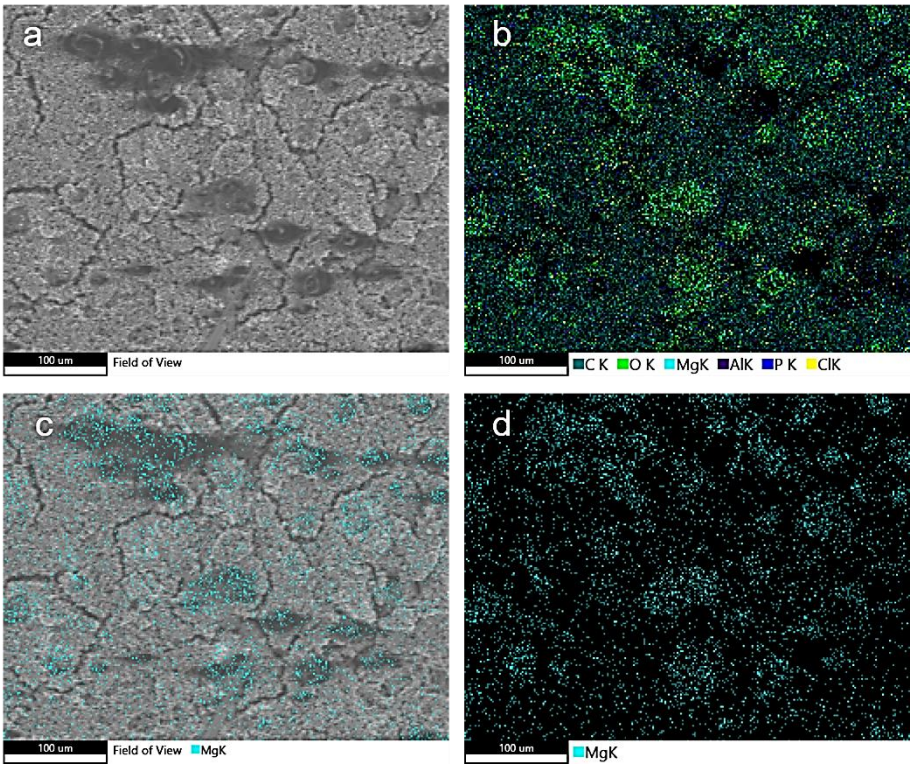

Supplementary Figure 23. Surface morphologies and corresponding EDS mappings of the cycled BP/carbon electrodes with Mg deposited capacities of 1.0 mAh cm^{-2}. The electrochemical tests were conducted at 25 °C using an APC electrolyte solution. **a**. SEM image. **b**. Combined EDS mapping. **c**. SEM image overlaid with Mg distribution mapping. **d**. Mg distribution mapping.

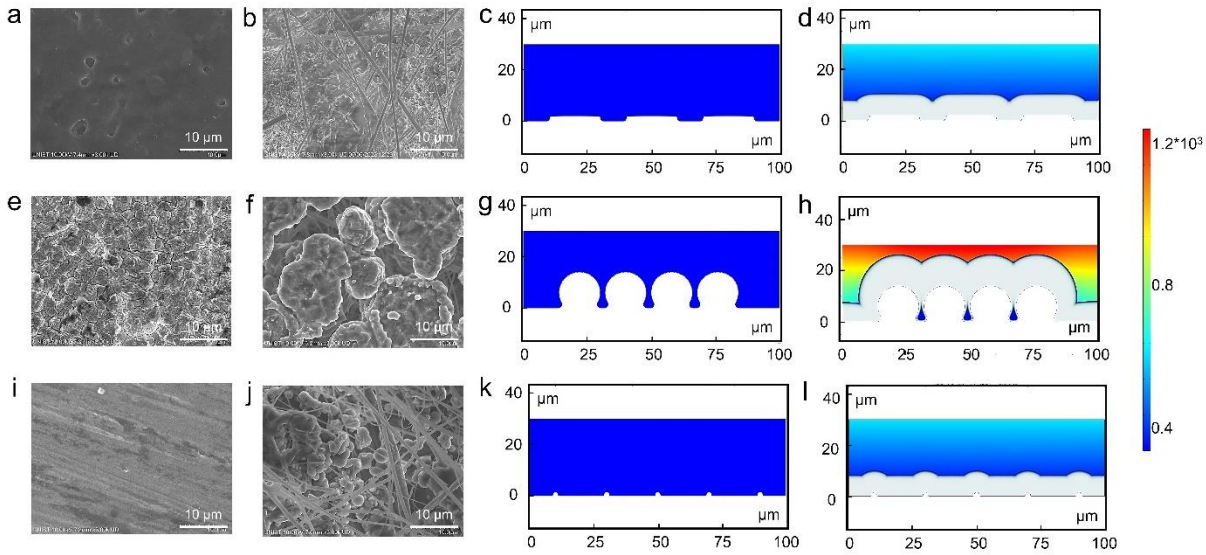

Supplementary Figure 24. SEM observation and theoretical simulation results of Mg deposition behaviors on different substrates. a–**d**, The BP electrode. **e**–**h** The Cu matrix, and **i-l**, Mg matrix. **a**, **e**, **i**, SEM images of the fresh matrices. **b**, **f**, **j**, SEM images of corresponding Mg deposition states. The colorful bar on the right is the surface electrolyte current density in the simulation results. **c**, **d**, **g**, **h**, **k**, **l**, Theoretical simulations showing the Mg deposition behaviors and the surface current densities (SCD) distributions during Mg deposition on the BP, Cu, and Mg matrices. The electrochemical tests were conducted at 25 °C using an APC electrolyte solution.

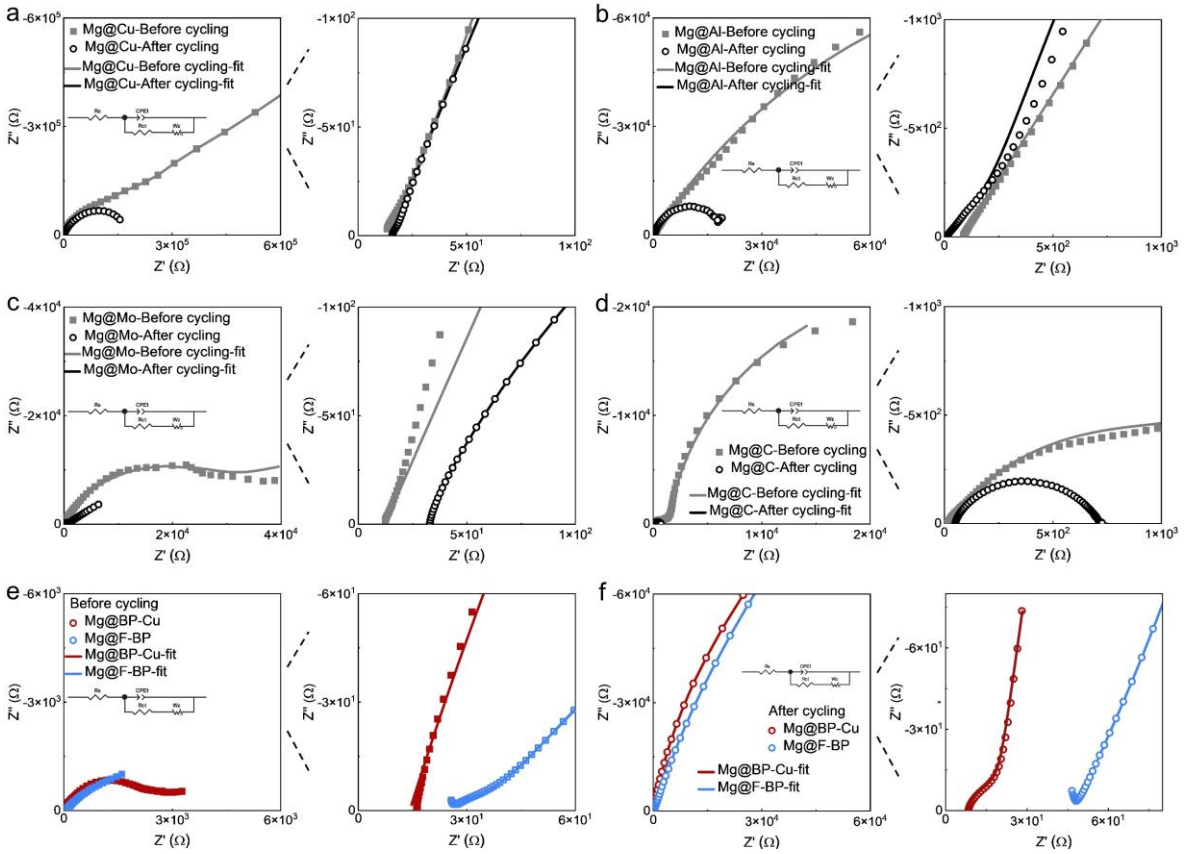

Supplementary Figure 25. Original and fitting EIS results of the symmetric Mg@M||Mg@M cells. a-d, Nyquist profiles. M refers to **a**, Cu, **b**, Al, **c**, Mo, **d**, carbon fabric. **e, f** Nyquist profiles of the symmetric Mg@BP-Cu||Mg@BP-Cu cell and Mg@F-BP||Mg@F-BP cell before and after cycling, respectively. Each figure on the right side is the enlarged view of the high frequency region. The equivalent circuit model of EIS results is shown as the inset of each figure. The electrochemical tests were conducted at 25 °C using an APC electrolyte solution.

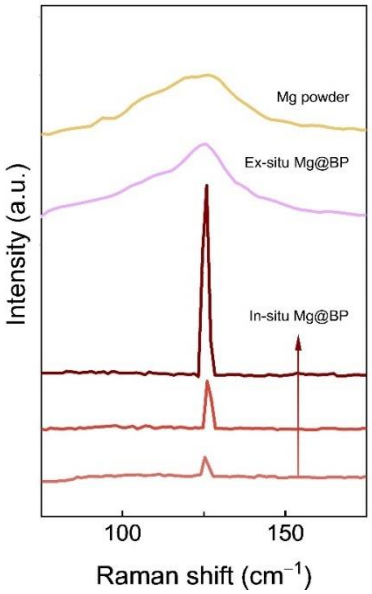

Supplementary Figure 26. Raman spectra of Mg powder, *ex situ* Mg@BP composite electrode, and *in situ* Mg@BP composite electrode tested in the *in situ* Raman spectroscopy. The electrochemical tests were conducted at 25 °C using an APC electrolyte solution.

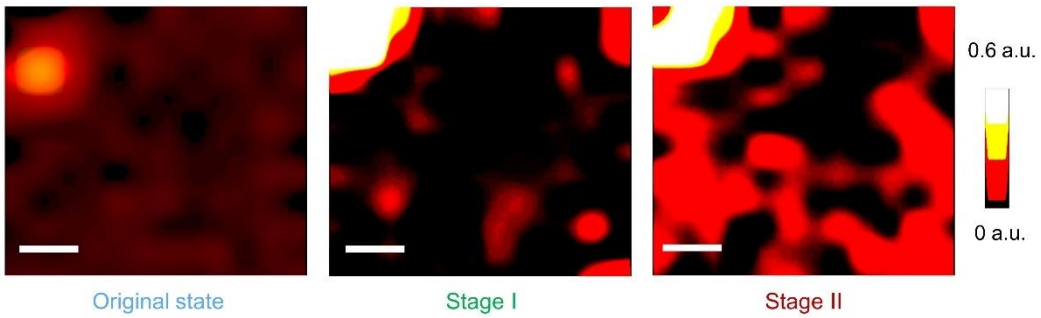

Supplementary Figure 27. Raman images during *in situ* Raman tests which recorded the Mg deposition process of the BP electrode. The scale bar is 1 μm. The *in situ* test was conducted using BP||Mg cell at 25 °C with an APC electrolyte solution.

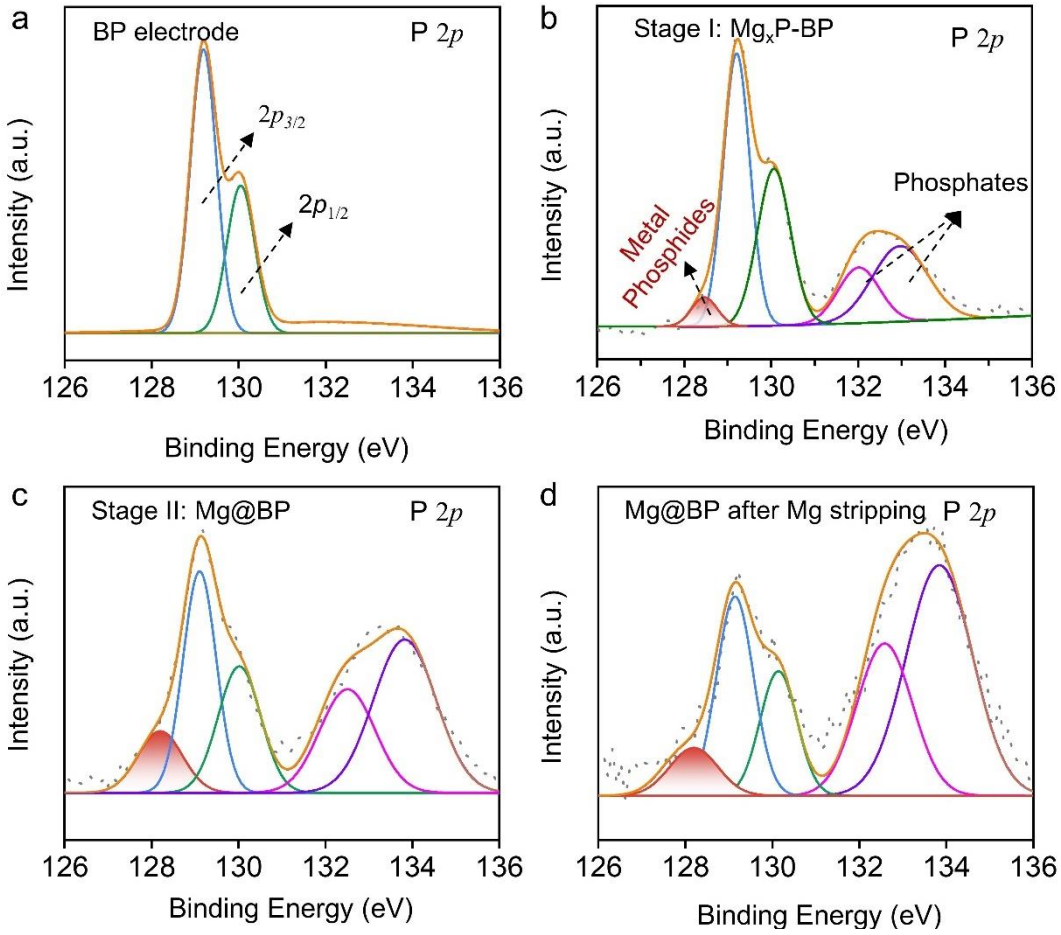

Supplementary Figure 28. XPS characterization of BP before and after Mg depositing and stripping. **P *2p* spectra**. **a**, pristine BP electrode, **b**, during Mg deposition process at Stage I, **c**, BP electrode after Mg deposition at Stage II, and **d** Mg@BP composite negative electrode after Mg stripping. The electrochemical tests were conducted using BP||Mg cells at 25 °C with an APC electrolyte solution.

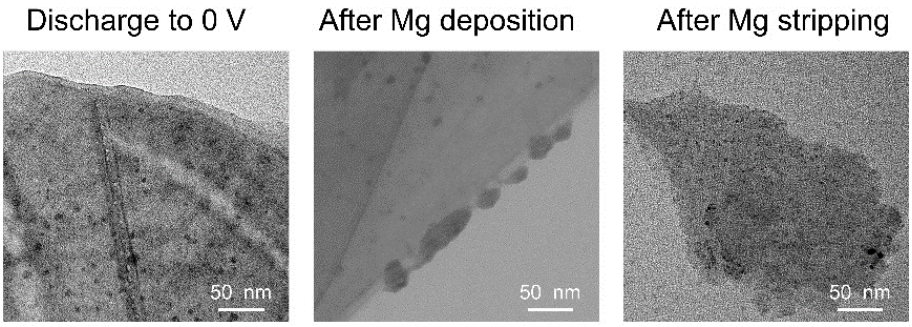

Supplementary Figure 29. TEM images of BP nanosheets at low magnification during Mg deposition. The morphologies after depositing and stripping were got from disassembling the cycled BP||Mg cell at 25 °C with an APC electrolyte solution.

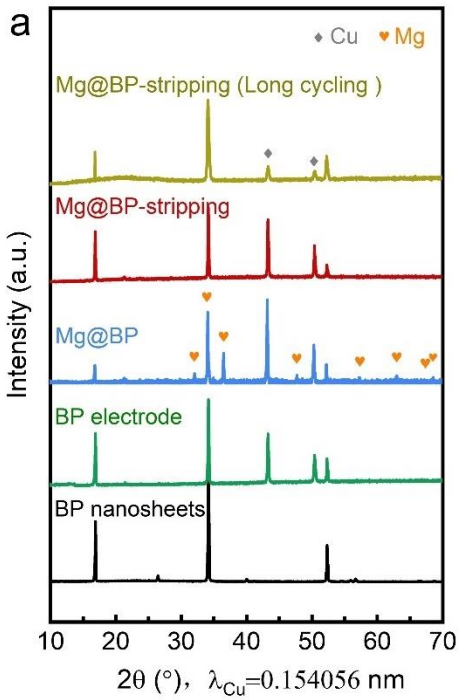

Supplementary Figure 30. XRD patterns of BP nanosheets, BP electrode, Mg@BP composite electrode, and Mg@BP composite electrode after Mg stripping in the first cycle and after long-time cycling. The Mg@BP, Mg@BP-stripping, Mg@BP-stripping (Long cycling) samples were got from disassembling the cycled BP||Mg cell at 25 °C with an APC electrolyte solution.

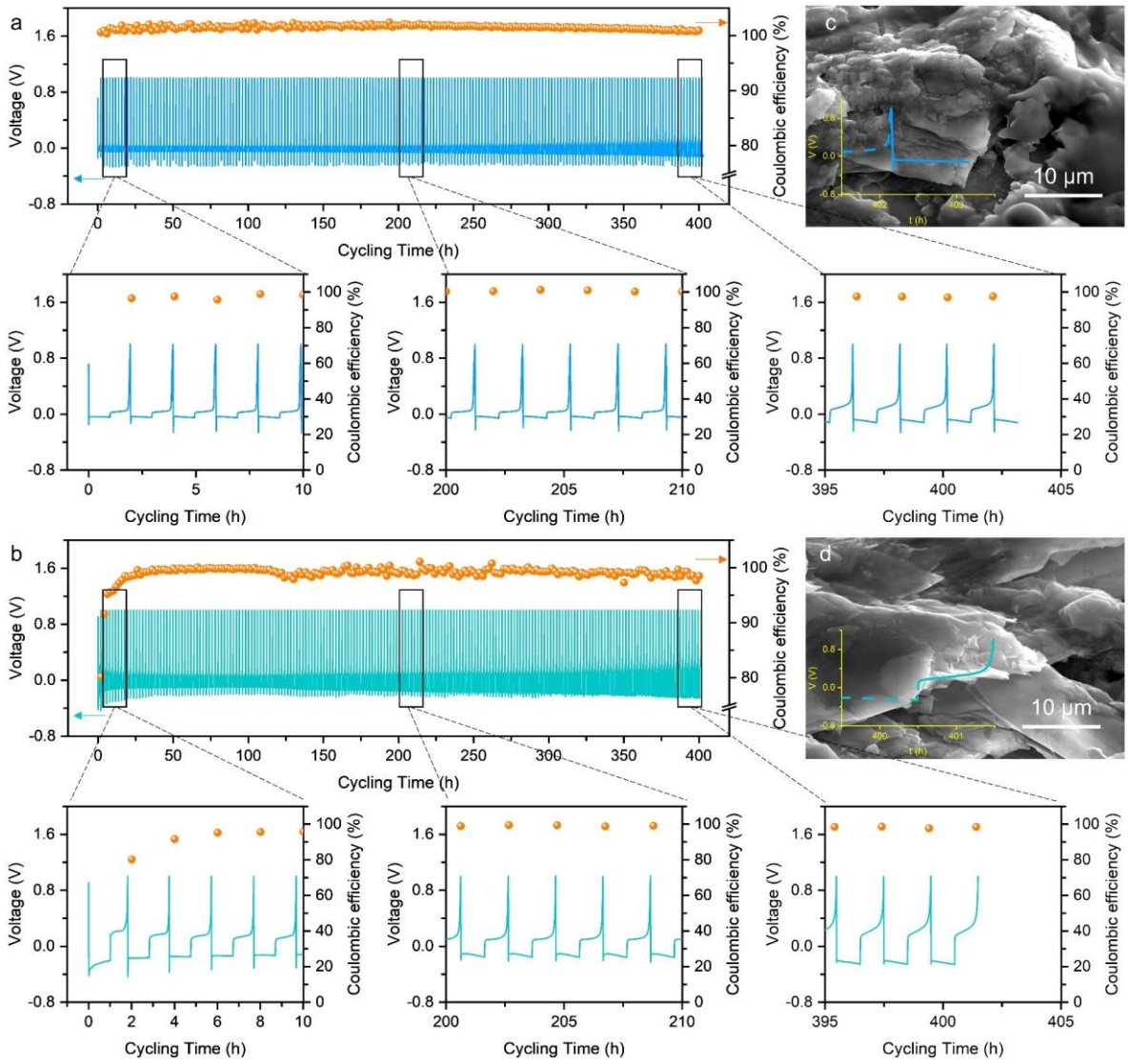

Supplementary Figure 31. Postmortem analysis of the Mg@BP composite electrode after long-time cycling. a, **b**, Long-time cycling voltage profiles of asymmetric BP||Mg cells. The cells had been cycled for 400 h at I_D of 3 mA cm^{-2} and C_c of 3 mAh cm^{-2}, and then stopped at **a**, Mg deposition state and **b**, Mg stripping state for the SEM postmortem analyses. **c**, **d**, SEM images of the above cycled Mg@BP composite negative electrode. **c**, at Mg plated state and **d**, at Mg stripped state. Insets in **c**, **d** are the enlarge voltage profiles before postmortem observations. All tests were conducted using BP||Mg cell at 25 °C with an APC electrolyte solution.

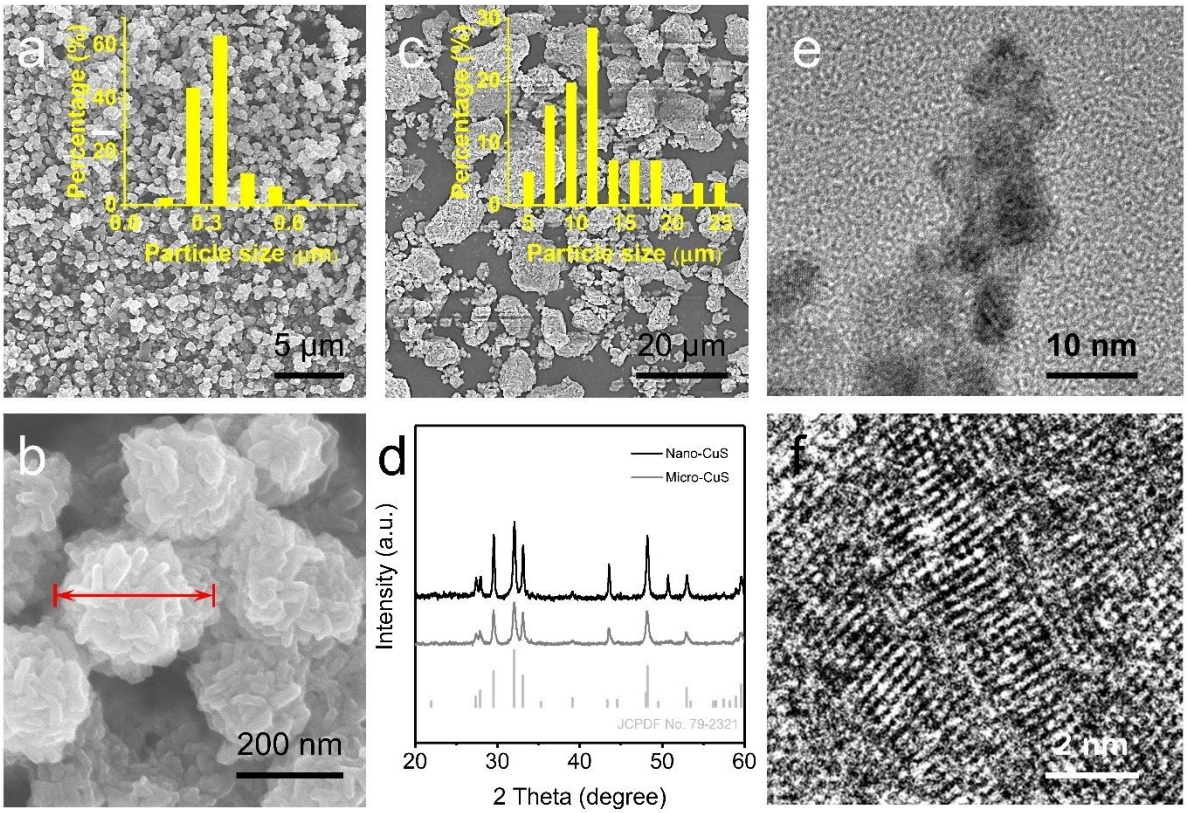

229

230 **Supplementary Figure 32. Material characterization of the nano-CuS and micro-CuS.**
231 SEM images: **a**, **b** nano-CuS. Insets show the particle distribution statistics. **c** Commercial
232 micro-CuS. d XRD results of nano-CuS and commercial micro-CuS. **e**, TEM and **f**, HR-TEM
233 images of the nano-CuS.

234

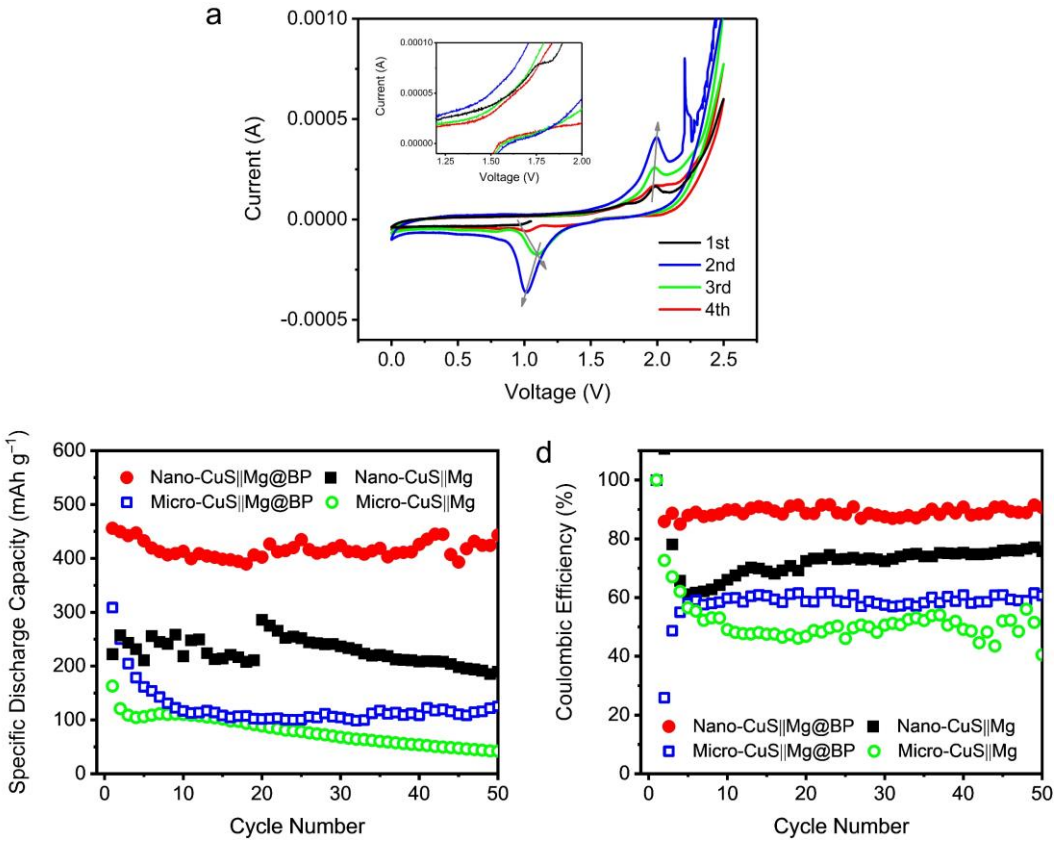

Supplementary Figure 33. Electrochemical performances of the nano-CuS and micro-CuS. CV profile of **a**, Mg||micro-CuS cell. **b**, Cycling performances and **c**, Corresponding Coumobic efficiency (CEs) of the micro-CuS||Mg, micro-CuS||Mg@BP, nano-CuS||Mg, and nano-CuS||Mg@BP cells at a specific current of 50 mA g^{-1}. All the tests were conducted at room temperature using an APC electrolyte solution.

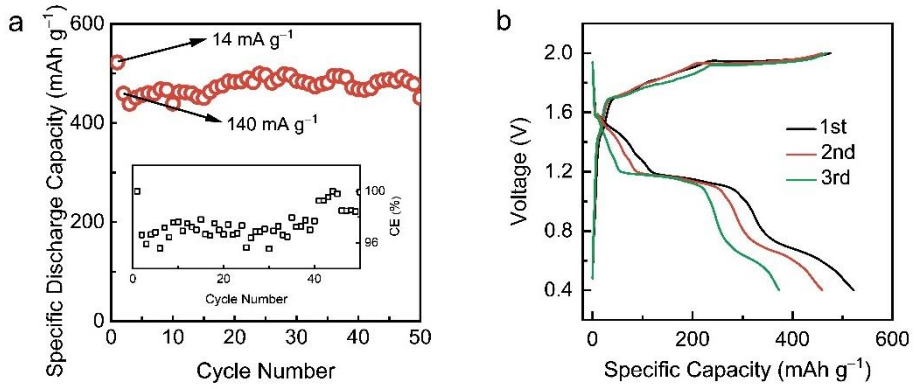

Supplementary Figure 34. The electrochemical performances of the BP@Mg||nano-CuS cell, using a stainless-steel current collector in the nano-CuS positive electrode. a, The cycling performance. The battery was activated at the specific current of 14 mA g^{-1} for the first cycle and then was cycled at specific current of 140 mA g^{-1} for the following cycles. The inset in **a** is the coulombic efficiency (CE). **b**, Voltage profiles during cycling. All the tests were conducted at 25 °C using an APC electrolyte solution.

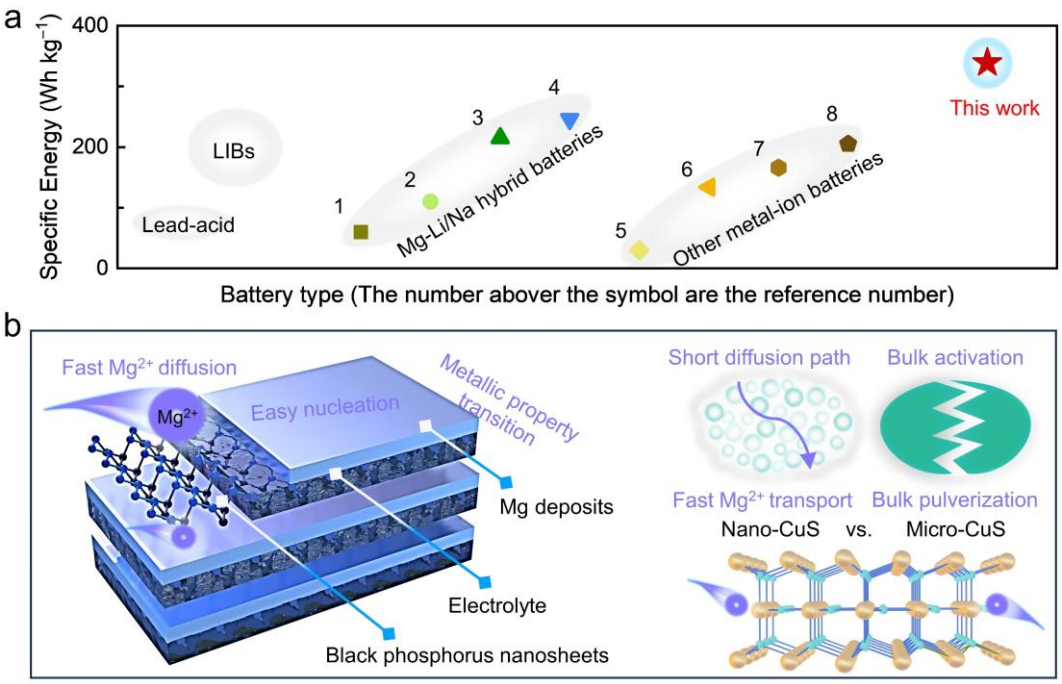

Supplementary Figure 35 Specific Energy evaluation and working mechanism illustration of the Mg@BP||nano-CuS full cell. a, Comparison of the specific energies of the Mg@BP||nano-CuS battery and other current full battery systems[1-8]. **b**, Schematic illustration of the Mg@BP composite negative electrode and the nano-CuS positive electrode.

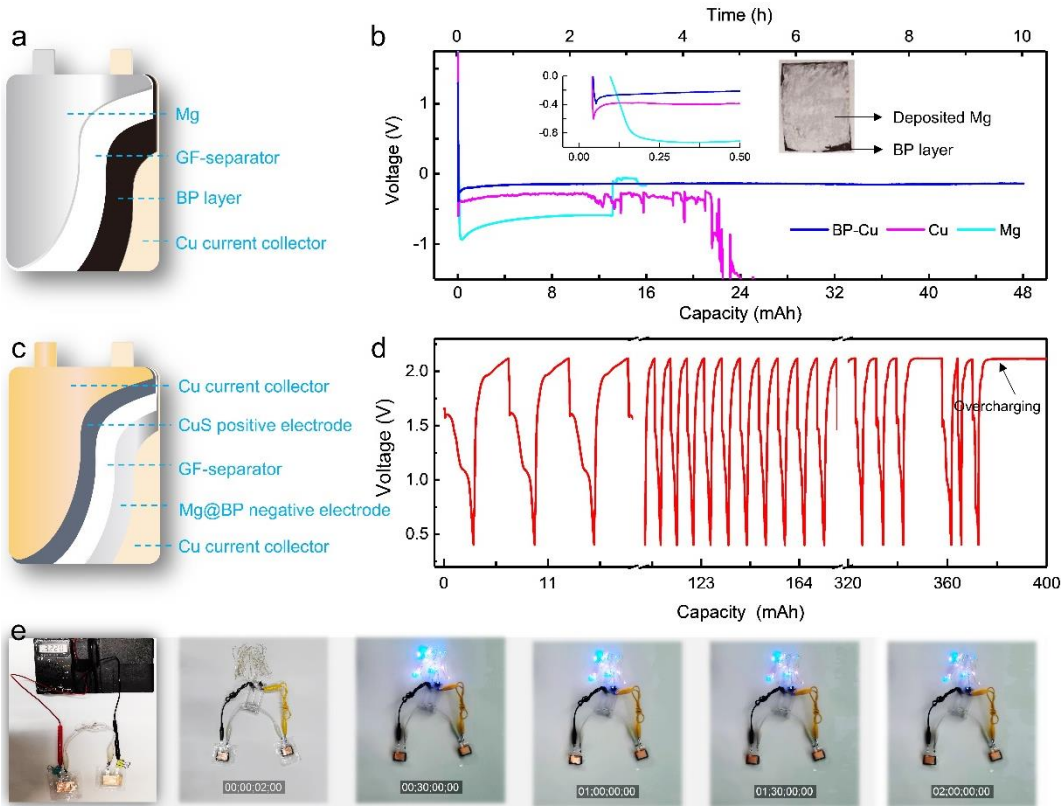

Supplementary Figure 36. Evaluation of the practical application potential of the composite Mg@BP negative electrode. a, Battery model of the BP||Mg cell for large area Mg@BP composite negative electrode preparation. The size of the electrodes was 3 cm × 2.5 cm. **b**, Corresponding voltage profiles of Mg deposition for the BP||Mg, Cu||Mg, and Mg||Mg batteries. Inset images in b show voltage profiles and an optical photograph of the Mg@BP negative electrode after Mg deposition. **c**, Model illustration of the soft-packaged Mg@BP||nano-CuS battery. **d**, Discharging and charging profiles of the soft-packaged Mg@BP||nano-CuS battery at specific current of 280 mA g^{-1}. **e**, Photographic pictures of Mg@BP||nano-CuS cells connected in series powering a string LED. All the electrochemical tests were conducted at 25 °C using an APC electrolyte solution.

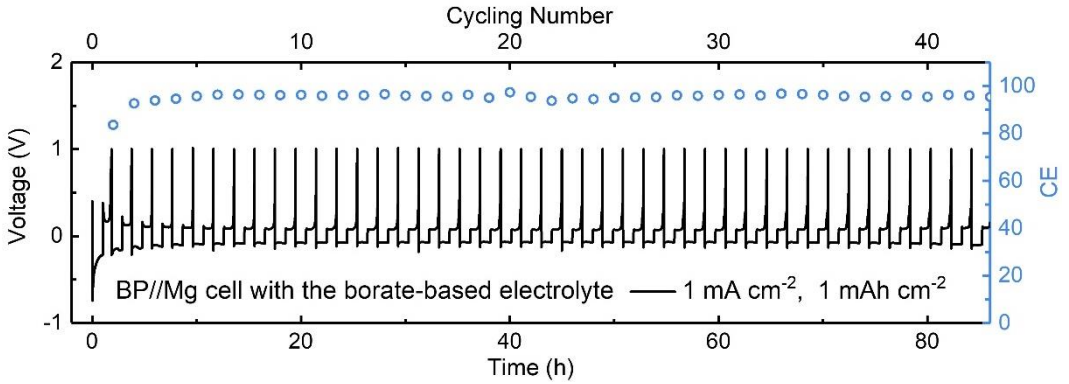

Supplementary Figure 37. Electrolyte compatibility of the BP electrode for Mg deposition with the borate-based electrolyte. The cycling performance and CEs of the asymmetric Mg||BP battery with the borate-based electrolyte at specific current of 1 mA cm^{-2} and areal capacity of 1 mAh cm^{-2}. The electrochemical test was conducted at 25 °C.

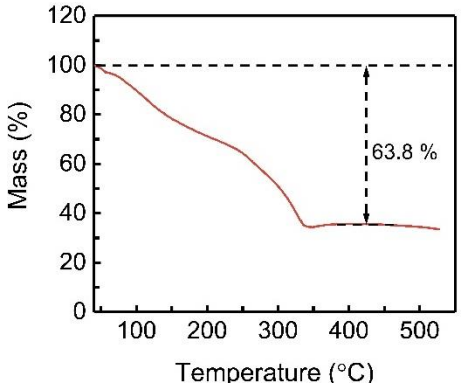

Supplementary Figure 38. TG result of the sulfur-based positive electrode which was peeled off from the carbon fabric current collector.

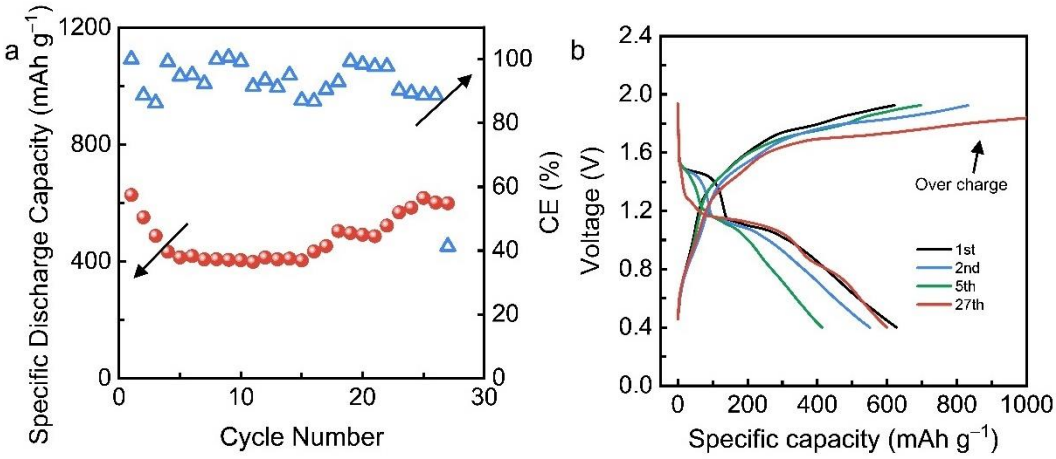

Supplementary Figure 39. Electrochemical performances of the Mg@BP||S battery. a, Cycling performance at specific current of 840 mA g^{-1}. b, Voltage profiles of the 1st 2nd, 5th and 27th cycle in **a**. All the electrochemical tests were conducted at room temperature using the borate-based electrolyte solution at 25 °C.

Supplementary Table 1. Physical and electrochemical properties of alkali metal and Mg electrodes [9-14]

Metal electrode	**Ionic radius** (pm)	**Charge density** (C mm^{-3})	**Abundance rank in earth crust**	**Cost** (USD kg^{-1})	**Reduction potential** (v.s. SHE)	**Theoretical mass capacity** (mAh g^{-1})	**Theoretical volumetric capacity** (mAh cm^{-3})
Li	76	52	33rd	165	-3.04	3840	2046
Na	102	24	6th	2.57–3.43	-2.71	1166	1131
K	138	11	7th	12.1–13.6	-2.93	685	589
Mg	**72**	**120**	**8th**	**2.2**	**-2.37**	**2205**	**3833**
Ca	99	52	5th	2.4	-2.87	1337	2073
Al	54	364	3rd	3.4	-1.66	2980	8040
Zn	74	112	9th	2.2	-0.76	820	5850

Supplementary Table 2. Comparison of the Mg planting capability of BP substrate in this work to the reported substrates. All the data including that from the references were achieved at room temperature.

Designed substrates	Asymmetric batteries performances					Symmetric cell performances
	I_D (mA cm^{-2})	C_c (mAh cm^{-2})	Cycling life (h)/(cycle)	CE (%)	Max I_D (mA cm^{-2})	Cycling life (h)/(cycle)
GC-NS[15] (*ACS Appl. Mater. Interfaces* 2019, 11, 38754−38761) (APC electrolyte)	2	0.2	200/1000	99.9	/	/
3D-VNCA[16] (*Adv. Mater.* 2021, 33, 2100224) (APC electrolyte)	10	0.2	40/100	/	5	70/168
3D-Au@PCNF[17] (*Chem. Eng. J.* 2022, 431, 13396) (APC electrolyte)	1	1	50/100	~95	/	/
Au-Cu[18] (*Nano Lett.* 2022, 22, 6808−6815) ((Mg(OTf)$_2$-based ether electrolyte)	1	1	1000/500	99.67	1	/
$Mo_2Ti_2C_3$[19] (*Small Methods* 2023, 7, 2201598) ((Mg(OTf)$_2$-based ether electrolyte)	3	3	420/210	99	15	/
$Ti_3C_2T_x$[20] (***Adv. Funct. Mater*. 2023, 33, 2303067**) ((Mg(OTf)$_2$-based ether electrolyte)	1	1	1000/500	99.2	/	/
	3	3	770/385	99.6		
	5	5	728/364	99.7		
BP in this work (APC electrolyte)	**2**	**2**	**1600/800**	**99.31**	**20**	**1000/500**
	4	**4**	**1400/700**	**99.66**		
	8	**8**	**1200/600**	**99.97**		
	16	**16**	**800/400**	**99.98**		
	8	**80**	**1100/50**	**96.65**		

Supplementary Table 3. R_s and R_{ct} of the symmetric Mg@M||Mg@M cells before and after cycling (M: Cu, Al, Mo, carbon fabric, or F-BP). F-BP refers to the freestanding BP membrane

Electrode	R_s (Ω)				R_{ct} (Ω)			
	Before value	Error	After value	Error	Before value	Error	After value	Error
Mg@Cu	2.2	0.6%	15.9	0.8%	2.1×10^5	0.7%	1.7×10^5	2.8%
Mg@Al	86.8	0.9%	12.2	1.1%	2.2×10^4	2.3%	2.0×10^4	0.8%
Mg@Mo	12.4	2.7%	32.7	2.9%	2.7×10^4	2.1%	9.5×10^2	1.6%
Mg@C	15.5	1.2%	49.4	0.6%	1.0×10^3	1.1%	6.1×10^2	0.4%
Mg@BP	**16.3**	**0.5%**	**8.7**	**1.9%**	**3.2×10^3**	**0.8%**	**24.9**	**2.1%**
Mg@F-BP	**25.7**	**1.6%**	**12.9**	**1.7%**	**34.5**	**1.9%**	**43.1**	**2.5%**

Supplementary Table 4. Chemical composition analysis of phosphide intermediates of Mg@BP composite electrode. Mg^{2+} was intercalated in BP electrode using a Mg||BP cell at room temperature and an APC electrolyte solution. The cut-off voltage was set as 0 V, referring to the end of stage I. Then, the cycled BP nanosheets were collected and adequately extracted with pure THF solvent for the ICP-OES analysis. All the tests were conducted at 25 °C using an APC electrolyte solution.

Element	Calc Conc. (ppm)	Molar ratio
P	81673	1
Mg	3847	0.06

Supplementary Note 1

The thickness of the BP nanosheets was determined by atomic force microscopy (AFM), as shown in Supplementary Fig. 1i. The AFM images and height profiles confirmed that the minimum height of the BP nanosheets is approximately 8 nm, while the maximum height is about 20 nm. Given that the thickness of a single-layer phosphorene is approximately 0.8 nm, it could be inferred that the prepared BP nanosheets consisted of ten to twenty-five stacked layers of phosphorene.

Supplementary Note 2

The feasibility of constructing the composite Mg electrode using other commonly used Cu, Al, Mo, and carbon fabric substrates were also investigated. Supplementary Fig. 10 showed the Mg plating and stripping performances of those substrates. The F-BP substrate exhibited stable cycling performance, maintaining a high coulombic efficiency of over 95% during cycling (Supplementary Fig. 10a–b), which was comparable to that of the BP electrode coated on the Cu current collector. In contrast, the commonly used substrates of Cu, Mo, Al, and carbon fabric substrates exhibited unstable cycling performances, and all experienced low CEs of less than 80%, or early short circuits during cycling, suggesting limited application possibilities in RMBs (Supplementary Fig. 10c–f). These results not only excluded the influence of the current collector of the BP electrode, but also confirmed the superiority of BP for constructing composite Mg negative electrode for full RMBs, even for future flexible ones.

Supplementary Note 3

As shown in Supplementary Fig. 16, SEM and EDS mapping results revealed that Mg was densely plated into the Mg@F-BP composite electrode as evidenced by the morphology change from a layer-stacked structure (F-BP) to a dense-packed structure with uniform P and Mg element distribution (Mg@F-BP composite negative electrode).

Supplementary Note 4

Because of the weak affinity of the Mg deposits on the Cu substrate, most of the Mg deposits attached on the glass fiber separator and easily detached from the Cu substrate during the cell disassembly process. Hence, micro-morphologies of the Mg deposits on glass fiber were checked in Supplementary Figure 17a, b to reveal the Mg deposition state on the Cu substrate. To fully reveal the morphologies of Cu after Mg deposition, Cu substrate in this postmortem analysis with little Mg deposits residue was also studied using SEM and mappings results, as shown in Supplementary Figure 18.

Supplementary Note 5

SEM and EDS results further revealed the Mg deposition behavior of different substrates, as depicted in Supplementary Fig. 20–21. Consistent with previous SEM observations (Supplementary Fig. 17–19), Mg was conformally deposited on the BP nanosheets of the F-BP electrode exhibiting a uniform and compact morphology (Supplementary Fig. 20a, 21a); Mg deposits easily detached from the Cu substrate and adhered to the surface of the glass fiber separator (Supplementary Fig. 20b–c, 21b). Additionally, uneven Mg agglomerations deposited on the Mo, Al, or carbon fabric substrates, consistent with their electrochemical cycling performances (Supplementary Fig. 10). The Mg deposition morphologies also explained the early short circuit phenomenon of the Al||Mg and C||Mg cells during cycling. Specifically, there were corrosion cracks evident on the Al substrate because of the interaction between Al and the aluminum complex in the electrolyte (Supplementary Fig. 20d and 21d)[9], which might lead to early short circuit during cycling. For the carbon fabric substrate, deposited Mg accumulated into large lumps (Supplementary Fig. 20f and 21f), increasing the risk of direct electrode contact and thus potentially causing an early short circuit.

Supplementary Note 6

As shown in Supplementary Fig. 22a, the BP nanosheets were evenly surrounded by carbon black nanoparticles in the BP/carbon electrodes. Severe nano-sized cracks formed, but the Mg deposition state was not obvious with a small deposition capacity from 0.125 to 0.5 mAh cm^{-2} (Supplementary Fig. 22b–d). When the deposition capacity increased to 1.0 mAh cm^{-2}, the nano-sized cracks were further enlarged, while Mg was conformally deposited on the BP nanosheets (Supplementary Fig. 22e, 23). The deposited Mg gradually fused and presented a dense surface morphology, when the deposition capacity further increased to 5.0 mAh cm^{-2} (Supplementary Fig. 22f), which was different from the deposition states on the Cu and Mg substrates (Supplementary Fig. 17). To conclude, the BP nanosheets exhibited better Mg affinity than both potential substrate materials (carbon material and Cu) and pristine Mg.

Supplementary Note 7

The P 2p photoelectron spectra of the BP nanosheets (Supplementary Fig. 28a) showed two spin-orbital splitting doublets located at 129.4 and 130.2 eV, which were associated with the $2p_{3/2}$ and P $2p_{1/2}$ orbitals of crystalline BP. During Mg plating process to prepare the Mg@BP composite negative electrode, metal phosphides located at 128.2 eV and phosphates in the range of 132−136 eV were detected at Stage I and Stage II (Supplementary Fig. 28b, c). The phosphates could be attributed to the degradation products of BP with the ambient oxygen. It was found that the photoelectron emission peaks of phosphide intermediates still existed after Mg stripping (Supplementary Fig. 28d), indicating that the intermediate formation reactions at the early stage of the deposition process were chemically irreversible.

Supplementary Movie 1 Two soft packaged full Mg@BP||nano-CuS cells powering a string of LEDs for 2 h.

References:

1. Li, Z., *et al.* Fast kinetics of multivalent intercalation chemistry enabled by solvated magnesium-ions into self-established metallic layered materials. *Nat. Commun.* **9**, 5115 (2018).
2. Chen, Z., *et al.* Fast magnesiation kinetics in α-Ag_2S nanostructures enabled by an in situ generated silver matrix. *Chem. Commun.* **55**, 4431-4434 (2019).
3. Walter, M., Kravchyk, K. V., Ibáñez, M., Kovalenko, M. V. Efficient and inexpensive sodium–magnesium hybrid battery. *Chem. Mater.* **27**, 7452-7458 (2015).
4. Cheng, Y., *et al.* Toward the design of high voltage magnesium–lithium hybrid batteries using dual-salt electrolytes. *Chem. Commun.* **52**, 5379-5382 (2016).
5. Monti, D., *et al*. Multivalent batteries—prospects for high energy density: Ca batteries. *Front. Chem.* **7**, 00079 (2019).
6. Liang, G., *et al.* Gradient fluorinated alloy to enable highly reversible Zn-metal anode chemistry. *Energ. Environ. Sci.* **15**, 1086-1096 (2022).
7. Mao, Y., *et al.* Foldable interpenetrated metal-organic frameworks/carbon nanotubes thin film for lithium–sulfur batteries. *Nat. Commun.* **8**, 14628 (2017).
8. Li, Y., *et al.* Interfacial engineering to achieve an energy density of over 200 Wh kg^{-1} in sodium batteries. *Nat. Energy* **7**, 511-519 (2022).
9. Y. Sun, F. Ai, Y.-C. Lu, Electrolyte and interphase design for magnesium anode: major challenges and perspectives. Small 18, 2200009 (2022).
10. T. Zhang et al. Degradation chemistry and stabilization of exfoliated few-layer black phosphorus in water. *J. Am. Chem. Soc.* 140, 7561-7567 (2018).
11. Liang, Y., Dong, H., Aurbach, D., Yao, Y. Current status and future directions of multivalent metal-ion batteries. *Nat. Energy* 5, 646-656 (2020).
12. Zhang, X., et al. Challenges and opportunities for multivalent metal anodes in rechargeable batteries. *Adv. Funct. Mater.* 30, 2004187 (2020).
13. Wang, M., Zhang, F., Lee, C. S., Tang, Y. Low‐cost metallic anode materials for high performance rechargeable batteries. *Adv. Energy Mater.* 7, 1700536 (2017).
14. Hwang, J. Y., Myung, S. T., Sun, Y. K. Recent progress in rechargeable potassium

batteries. *Adv. Funct. Mater.* 28, 1802938 (2018).

15. Lim, H. D., et al. Magnesiophilic Graphitic carbon nanosubstrate for highly efficient and fast-rechargeable Mg metal batteries. *ACS Appl. Mater. Interfaces* 11, 38754-38761 (2019).

16. Song, Z., Zhang, Z., Du, A., Dong, S., Li, G., Cui, G. Uniform magnesium electrodeposition via synergistic coupling of current homogenization, geometric confinement, and chemisorption effect. *Adv. Mater.* 33, e2100224 (2021).

17. Lee, S., et al. Gold-incorporated porous hollow carbon nanofiber for reversible magnesium-metal batteries. *Chem. Eng. J.* 431, (2022).

18. Li, Y., et al. High utilization of composite magnesium metal anodes enabled by a magnesiophilic coating. Nano Lett. 22, 6808-6815 (2022).

19. Li, Y., et al. Double-transition-metal mxene films promoting deeply rechargeable magnesium metal batteries. *Small Methods* 7, e2201598 (2023).

20. Li, Y., et al. MXene‐based anode‐free magnesium metal battery. *Adv. Funct. Mater.* 33, 2303067 (2023).